

AEDC-TR-94-14

**Analysis of Planar Laser-Induced Fluorescence
Images Obtained During Shakedown Testing of
the AEDC Impulse Facility**

**W. M. Ruyten, W. D. Williams, and F. L. Heltsley
Micro Craft Technology/AEDC Operations**

March 1995

Final Report for Period October 1993 — September 1994

Approved for public release; distribution is unlimited.

**ARNOLD ENGINEERING DEVELOPMENT CENTER
ARNOLD AIR FORCE BASE, TENNESSEE
AIR FORCE MATERIEL COMMAND
UNITED STATES AIR FORCE**



NOTICES

When U. S. Government drawings, specifications, or other data are used for any purpose other than a definitely related Government procurement operation, the Government thereby incurs no responsibility nor any obligation whatsoever, and the fact that the Government may have formulated, furnished, or in any way supplied the said drawings, specifications, or other data, is not to be regarded by implication or otherwise, or in any manner licensing the holder or any other person or corporation, or conveying any rights or permission to manufacture, use, or sell any patented invention that may in any way be related thereto.


Qualified users may obtain copies of this report from the Defense Technical Information Center.

References to named commercial products in this report are not to be considered in any sense as an endorsement of the product by the United States Air Force or the Government.

This report has been reviewed by the Office of Public Affairs (PA) and is releasable to the National Technical Information Service (NTIS). At NTIS, it will be available to the general public, including foreign nations.

APPROVAL STATEMENT

This report has been reviewed and approved.



GARY R. MATTASITS
Technical Director
Space and Missile Systems Test Division

Approved for publication:

FOR THE COMMANDER



CONRAD M. RICHEY, LtCol, USAF
Chief, Space and Missile Test Division
Operations Directorate

REPORT DOCUMENTATION PAGE			<i>Form Approved</i> <i>OMB No. 0704-0188</i>	
Public reporting burden for this collection of information is estimated to average 1 hour per response, including the time for reviewing instructions, searching existing data sources, gathering and maintaining the data needed, and completing and reviewing the collection of information. Send comments regarding this burden estimate or any other aspect of this collection of information, including suggestions for reducing this burden, to Washington Headquarters Services, Directorate for Information Operations and Reports, 1215 Jefferson Davis Highway, Suite 1204, Arlington, VA 22202-4302, and to the Office of Management and Budget, Paperwork Reduction Project (0704-0188), Washington, DC 20503.				
1 AGENCY USE ONLY (Leave blank)		2 REPORT DATE March 1995		3 REPORT TYPE AND DATES COVERED Final - October 1993 - September 1994
4. TITLE AND SUBTITLE Analysis of Planar Laser-Induced Fluorescence Images Obtained During Shakedown Testing of the AEDC Impulse Facility			5. FUNDING NUMBERS 0129	
6. AUTHOR(S) W. M. Ruyten, W. D. Williams, and F. L. Heltsley Micro Craft Technology, AEDC Operations				
7 PERFORMING ORGANIZATION NAME(S) AND ADDRESS(ES) Arnold Engineering Development Center/DOS Air Force Materiel Command Arnold Air Force Base, TN 37389-4000			8. PERFORMING ORGANIZATION (REPORT NUMBER) AEDC-TR-94-14	
9 SPONSORING/MONITORING AGENCY NAME(S) AND ADDRESS(ES) Arnold Engineering Development Center/DOS Air Force Materiel Command Arnold Air Force Base, TN 37389-4000			10 SPONSORING/MONITORING AGENCY REPORT NUMBER	
11 SUPPLEMENTARY NOTES Available in Defense Technical Information Center (DTIC).				
12A DISTRIBUTION/AVAILABILITY STATEMENT Approved for public release; distribution is unlimited.			12B DISTRIBUTION CODE	
13 ABSTRACT (Maximum 200 words) Following a proof-of-principle demonstration of Planar Laser-Induced Fluorescence (PLIF) in the AEDC Impulse Facility in FY93, a set of four PLIF images was obtained during FY94 runs of the facility. The images were obtained away from the nose region of a spherically blunt cone, using excitation of nitric oxide in the flow. Two laser sheet geometries were employed and two excitation wavelengths were used. A procedure was developed whereby calibration images allow the remapping of the PLIF images to test article coordinates. Using this technique, it was shown that the bow shock positions determined by PLIF agree well with the shock positions measured using schlieren photography. More importantly, the set of PLIF images constitutes an initial database against which Computational Fluid Dynamics calculations of high enthalpy flows can be compared. Initial results of such a comparison, obtained through Computational Flow Imaging, are reported. Recommendations are given for future PLIF applications at the Impulse Facility.				
14 SUBJECT TERMS flow imaging planar laser-induced fluorescence hypersonic flow			15. NUMBER OF PAGES 64	
			16 PRICE CODE	
17 SECURITY CLASSIFICATION OF REPORT UNCLASSIFIED			18 SECURITY CLASSIFICATION OF THIS PAGE UNCLASSIFIED	
19 SECURITY CLASSIFICATION OF ABSTRACT UNCLASSIFIED			20 LIMITATION OF ABSTRACT SAME AS REPORT	

PREFACE

The work reported here was done at the Arnold Engineering Development Center (AEDC), Air Force Materiel Command (AFMC), Arnold AFB, TN. The AF project manager was Gary R. Mattasits; the manuscript was submitted for publication on March 1, 1995

The authors acknowledge the contributions of R. L. Clippard, J. H. Jones, B. J. McClure, J. R. Maus, L. L. Price, S. G. Rock, M. S. Smith, and J. T. Tarvin in various stages of this work.

CONTENTS

1.0	INTRODUCTION.....	5
2.0	SUMMARY OF EXPERIMENTAL RESULTS	5
3.0	COMPARISON WITH SCHLIEREN IMAGES	7
4.0	TRANSFORMATION FROM CAMERA TO TEST ARTICLE COORDINATES	8
5.0	REMAPPING OF A PLIF IMAGE TO TEST ARTICLE COORDINATES	10
6.0	BACKGROUND SUBTRACTION AND FLAT-FIELD CORRECTION	11
7.0	PLIF IMAGES FOR RUNS 16 AND 19	12
7.1	Run 16	12
7.2	Run 19	14
8.0	PLIF IMAGES FOR RUNS 14 and 15.....	15
8.1	Run 14	15
8.2	Run 15	16
9.0	DISCUSSION AND SUMMARY	18
	REFERENCES	19

ILLUSTRATIONS

<u>Figure</u>	<u>Page</u>
1. PLIF Experimental Setup at Impulse Facility.....	21
2. Schematic of Test Article	22
3. Laser Sheet Geometries Relative to Test Article	22
4. Schlieren Image for Run 16	23
5. Result of Digitizing and Fitting of Schlieren Shock Position for Run 16.....	24
6. Fitted Schlieren Shock Positions for Runs 14, 15, and 16	24
7. Image of Calibration Target Used for Run 15.....	25
8. Image of Calibration Target Used for Run 16.....	25
9. Back-Lit Image of the Test Article for Run 15.....	26
10. Definition of Camera Orientation Relative to Test Article Coordinate System	26
11. Comparison of Selected and Fitted Marks for Calibration Image from Fig. 7	27
12. Overlay of Fitted Test Article Features on Calibration Image from Fig. 8.....	27
13. Examples of Projections of Remapped Image Pixel Onto Original Image Grid	28
14. Flat-Field Calibration Image Obtained with Continuous Light Source and Long Gate	29
15. Typical Flat-Field Calibration Image Obtained with a Short Laser Pulse and a Short Gate	29
16. Raw PLIF Image for Run 16.....	31

<u>Figure</u>	<u>Page</u>
17. Run 16 PLIF Image Overlaid with Projection of Model and Shock.....	31
18. Average Horizontal Profile of Free-Stream Region in Fig. 16.....	33
19. Remapped, Energy-Normalized PLIF Image for Run 16.....	33
20. Average Radial PLIF Profiles through the Center of Fig. 19.....	35
21. Raw PLIF Image for Run 19.....	37
22. Remapped, Energy-Normalized PLIF Image for Run 19.....	37
23. Temperature Dependence of the PLIF Signal for the Two Transitions Used in this Work.....	39
24. Average Radial PLIF Profiles through the Center of Fig. 22.....	40
25. Raw PLIF Image for Run 14.....	41
26. Average Horizontal Profile of the Raw Image from Fig. 25.....	41
27. Energy-Normalized PLIF Image for Run 14.....	43
28. Average Vertical Profile of the PLIF Signal in Fig. 27.....	43
29. Expected Projections of the Intersection of the Laser Sheet with the Shock, as seen by the Camera for Run 14, for Various Distances Between Laser Sheet and Edge of the Model.....	45
30. Overlay of Selected and Fitted Intersection Points Between Laser Sheet and Shock on Energy-Normalized PLIF Image from Fig. 27.....	45
31. Fitted Laser Sheet Position for Run 14 Shown in Test Article Coordinates.....	46
32. Remapped, Energy-Normalized PLIF Images for Run 14.....	47
33. Raw PLIF Image for Run 15.....	49
34. Average Horizontal Profile of the Raw Image from Fig. 33.....	49
35. Energy-Normalized PLIF Image for Run 15.....	51
36. Average Vertical Profile of the PLIF Signal in Fig. 35.....	51
37. Overlay of Selected and Fitted Intersection Points Between Laser Sheet and Shock on Energy-Normalized PLIF Image from Fig. 35.....	53
38. Fitted Laser Sheet Positions for Run 15 Shown in Test Article Coordinates.....	53
39. Remapped, Energy-Normalized PLIF Images for Run 14.....	55
40. Detail Region of Fig. 39b.....	57

TABLE

	<u>Page</u>
1. Fitted Coefficients for Schlieren Shock Positions.....	59
NOMENCLATURE.....	60

1.0 INTRODUCTION

Planar Laser-Induced Fluorescence (PLIF) imaging has, in recent years, been shown to be a powerful non-intrusive diagnostic technique for the study of aerodynamic flow phenomena. In particular, PLIF has the potential of rendering instantaneous measurements of temperature and density fields in the flow. However, the application of the technique in a complex facility poses many challenges, from the perspectives of experimental complexity as well as data analysis. Thus it was a significant achievement when it was demonstrated in FY93 that it is possible to obtain PLIF images in the AEDC Impulse Shock Tunnel. In particular, PLIF images were obtained in the nose region of a blunt cone test article.

Here the development of image analysis techniques for the quantitative interpretation of such PLIF images is reported. In particular, the analyses of the PLIF images which were obtained during FY94 shakedown testing and evaluation of the Impulse Facility (Runs 14, 15, 16, and 19) are described. These images were also obtained with a blunt cone test article, but away from the nose region.

Two distinct categories of image analysis can be distinguished: (1) normalization and scaling and (2) derivation of flow properties. Analysis in the first category does not require specific knowledge of the flow under study, but is indispensable for the quantitative interpretation of the images. It involves correcting the image for imperfections in the camera and the laser sheet, and it involves geometric scaling to relate image pixel coordinates to test article coordinates. This report is concerned mostly with analysis in this category.

Work in the second category has, for this study, taken the form of Computational Flow Imaging (CFI). That is, synthetic PLIF images were generated from Computational Fluid Dynamics (CFD) solutions of the Impulse Facility flow around the test article, and these were compared with the experimental PLIF images after normalization and scaling. The results of the CFI-PLIF analysis have been documented in Ref. 1 and will be described only briefly in this report.

2.0 SUMMARY OF EXPERIMENTAL RESULTS

Figure 1 shows a schematic of the experimental setup (Ref. 2). Figure 2 shows a schematic of the test article used in the PLIF studies. A pulsed, wavelength-tunable UV laser beam was formed into a thin sheet and directed vertically into the Impulse Tunnel through an optical port at the top of the facility. The width of the sheet at the location of the test article was approximately 100 mm; the thickness of the sheet was less than 1 mm. The laser was tuned to a particular absorption line of the nitric oxide (NO) molecule. Two transitions were used in this work: (1) the 225.716 nm $R_{11}+Q_{21}(13.5)$ transition of the Gamma (0-0) band (Runs 14, 15, and 16); and (2) the 225.987

nm $R_{11}+Q_{21}(7.5)$ transition of the same band (Runs 17, 18, and 19). These lines were chosen because they provide relatively strong fluorescence signals and because they are well isolated spectrally from other absorption features in the Gamma (0,0) band.

The resulting fluorescence signals were recorded using an image-intensified CCD camera, with an array size of 578×384 pixels and a 14-bit digitizer readout. The camera was mounted to the side of the tunnel, with a line of sight at an angle of about 24 deg off-perpendicular to the centerline of the flow. Perpendicular viewing of the laser sheet would have been preferable, but the optical ports perpendicular to the flow were used by a schlieren imaging system. UV-pass filters were mounted on the camera to minimize the unintentional imaging of scattered laser light and spontaneous (non-laser-induced) emissions from the flow. Moreover, a short gate width (25 nsec for Run 14; 50 nsec for all other images) was chosen for the intensifier on the CCD camera to limit the contribution of spontaneous flow emission. This gate time is also short enough that the resulting image is essentially frozen in time: at a typical flow velocity of 4500 m/sec, a 50 nsec gate would cause maximum blurring of 0.23 mm; the actual blurring should be even less as a result of centering of the laser pulse within the gate and collisional quenching of the laser-excited state.

Despite the short gate width and the spectral filtering of the signal, spontaneous flow emission was found to dominate the signal in the nose region of the test article in an initial PLIF survey for Run 13 (see Ref. 2, Fig. 1). Thus, emphasis in this work was placed on obtaining high-quality PLIF images a few inches downstream from the nose region.

Six Impulse Facility runs were conducted during this study (Runs 14 through 19). The PLIF system was operated for each of these runs. However, no triggers were received for runs 17 and 18 so that no PLIF images are available for these. In Runs 14 and 15, the laser sheet was aligned parallel to the model surface, so as not to be intercepted by the test article (Fig. 3a). For Runs 16 and 19, the laser sheet was aligned along the meridian plane of the test article, impinging on the conical surface of the test article as shown in Fig. 3b.

Analysis of the PLIF images for Runs 14 and 15 is complicated by the fact that it appears that, in both images, the position of the laser sheet moved significantly from the original alignment position. After noting this problem on Run 15, the laser sheet optics were fastened more securely for subsequent runs, and no changes in alignment were seen as a result of the Impulse Facility firings for Runs 16 and 19.

3.0 COMPARISON WITH SCHLIEREN IMAGES

Schlieren images were obtained for most of the Impulse Facility runs. Although not specifically intended for this purpose, they were used to verify that shock locations in the PLIF images agree with those in the schlieren images for the same runs. This was accomplished as follows. First, a schlieren image (the one for Run 16 is shown in Fig. 4) was put on a digitizing tablet, and two series of points were selected manually: one along the model surface of the test article, the other along the bow shock.

Next, the digitizer tablet's model surface coordinates were least-squares curve-fitted to the known mathematical definition of the model surface, which is given by:

$$y = \begin{cases} \pm\sqrt{R^2 - x^2}; & x < -R \sin \alpha, \\ \pm(R + x \sin \alpha) / \cos \alpha; & x \geq -R \sin \alpha, \end{cases} \quad (1)$$

where $\alpha = 10^\circ$ is the half angle of the blunt cone, $R = 0.7$ in. is the radius of the spherical nose section, and the origin ($x = y = 0$) is located at the center of the spherical nose section. The scaling transformation from test article coordinates to digitizer tablet coordinates is determined by four fit parameters: a linear zoom factor, a horizontal and a vertical offset, and a rotation angle. After obtaining these fit parameters, the digitizer tablet's coordinates for the shock position could be transformed to test article coordinates by applying the inverse transformation.

Finally, the schlieren-derived shock positions were cast into parametric form by fitting the test article coordinates of the shock to the empirical equation

$$y = \pm \left[\frac{1}{b} (a + x + cx^2) \right]^{(1/\lambda)}, \quad (2)$$

where a , b , c , and λ are the parameters of the least-squares fit. As an example, Fig. 5 shows the theoretical model surface, the fitted shock location, and the rescaled digitizer coordinates for the schlieren image obtained during Run 16. Fitted values of the parameters a , b , c , and λ for Runs 14, 15, and 16 are given in Table I (valid for x and y in mm). These parameters are highly correlated. Thus significant differences between the fit parameters are not necessarily indicative of large variations in shock position. This is evident in Fig. 6, in which the fitted schlieren shock positions are shown for Runs 14, 15, and 16.

Finally it is noted that the above equation for the schlieren shock position is symmetric around the centerline ($y = 0$) by definition. However, slight deviations from symmetry were seen in the digitized shock positions (Fig. 5) as well as in the schlieren images themselves (Fig. 4). Thus it appears that some flow asymmetry was present.

4.0 TRANSFORMATION FROM CAMERA TO TEST ARTICLE COORDINATES

To establish the coordinate transformation between camera pixel coordinates and test article coordinates, two calibration images were typically obtained prior to an Impulse Facility run. The first was an image of a calibration target, consisting primarily of a rectangular array of marks; the second image was either a front-lit or back-lit image of the actual test article in which the model edges can be clearly discerned.

The calibration targets were placed at the anticipated positions of the laser sheets. In this work, a target consisting of an array of equally spaced rectangular dots was used. Some horizontal and vertical crosshair lines were marked on the target as well. Figures 7 and 8 show examples of the resulting target images for Runs 15 and 16. In Fig. 7, the target was placed at the pre-run laser sheet position shown in Fig. 2a; that is, it was aligned parallel to the model surface. In Fig. 8, the target was cut at a 10-deg angle and placed on top of the test article, aligned along the meridian plane of the test article (Fig. 3b). In both cases, the horizontal alignment of the target relative to the test article was achieved by centering the copper-stainless joint on the test article (3 in. from the model nose) between two of the vertical cross hairs in the target (in the case of Fig. 7, this alignment was facilitated by a small hole in the target). Figure 9 shows the back-lit image of the test article for Run 15. Because the model edge is visible in Fig. 8, no separate back-lit image was required.

Because the camera is mounted about 24 deg off-perpendicular, the horizontal features in the calibration images of Figs. 7 and 8 are seen to converge to the left. This results in a nonlinear transformation between object and image coordinates. To describe this transformation, the analysis was generalized to the case where the off-perpendicular viewing angle of the camera is given by an arbitrary angle, γ , and the viewing direction is pitched away from the horizontal plane by an (small, unintended) angle, δ (Fig. 10). Furthermore, the camera was assumed to be pointed (and focused) at some reference point (x_0, y_0, z_0) , to be removed by a distance, D , from this reference point, and to have associated with it an effective zoom factor, p . Neglecting aberration, the image of an arbitrary point (x, y, z) may now be expressed in terms of camera pixel coordinates (x_p, y_p) as

$$\begin{aligned}
x_p &= \frac{p (\vec{w} \cdot \hat{e}_x)}{D - (\vec{w} \cdot \hat{e}_n)}, \\
y_p &= \frac{p (\vec{w} \cdot \hat{e}_y)}{D - (\vec{w} \cdot \hat{e}_n)},
\end{aligned}
\tag{3}$$

where \hat{e}_x , \hat{e}_y , and \hat{e}_z are mutually orthonormal unit vectors given by

$$\begin{aligned}
\hat{e}_x &= (\cos \gamma, 0, -\sin \gamma) \\
\hat{e}_y &= (-\sin \gamma \sin \delta, \cos \delta, -\cos \gamma \sin \delta) \\
\hat{e}_n &= (\sin \gamma \cos \delta, \sin \delta, \cos \gamma \cos \delta)
\end{aligned}
\tag{4}$$

(these vectors are oriented, respectively, along the x and y axes of the camera and along the camera viewing direction), and w is the vector given by

$$\vec{w} = (x_0 - x, y_0 - y, z_0 - z).
\tag{5}$$

The parameters which must be determined on the basis of the calibration images are the angles γ and δ , the distance D , the zoom factor p , and the components of the reference point, x_0 , y_0 , and z_0 . This was accomplished through a least-squares fitting program, which takes as input the image centers of the marks in the calibration target and the image coordinates of the model edges. Both sets of coordinates were determined from the calibration images through a semi-automatic procedure in which the analyst pulls the image up on a computer screen and manually selects points of interest (either dot centers or edge points), which are then optimized automatically by dot-centering or edge-centering algorithms in the analysis software (further details can be provided on request).

As a check on this procedure, it is good practice to compare the input coordinates and fitted coordinates. Typically, an average fit error on the order of a one pixel separation was found to result. As an example, Fig. 11 shows the input and fitted coordinates of the centers of the reference marks from the calibration image in Fig. 7. (In Fig. 7, there is also a slight vertical misalignment between the camera and the calibration target; this could be compensated for by including a "roll" angle ϕ in the above equations. However, this inclusion was determined not to have a significant effect on the eventual remapping of the PLIF images.) Similarly, Fig. 12 shows the projected model position (edges, centerline, and model joint at 3 in. from the nose) as an overlay on Fig. 8. Note the good alignment of the projected features with those in the image.

5.0 REMAPPING OF A PLIF IMAGE TO TEST ARTICLE COORDINATES

Having established the transformation from test article coordinates to image pixel coordinates, two approaches can be taken. The simplest of these is to project a known feature in the flow onto the PLIF image. This approach proved very useful in checking for misalignment effects of the actual PLIF image relative to the pre-run calibration images. It was also instrumental in establishing the actual position of the laser sheet for Runs 14 and 15, where motion of the laser sheet during the Impulse Facility run appears to have taken place (see Sec. 8.0).

More generally, the coordinate transformation between test article coordinates and image coordinates can be used to remap a PLIF image to test article coordinates, and to undo the nonlinear mapping which is introduced by the off-perpendicular viewing direction of the camera. Specifically, when the position of the PLIF laser sheet is known (for example, $z = 0$ for Runs 16 and 19, and $z = a_s x + b_s y$ for Runs 14 and 15, where a_s and b_s are known), it is possible to invert Eqs. (3, 4, and 5), yielding test article coordinates (x, y, z) in terms of image pixel coordinates (x_p, y_p) . Schematically, this may be expressed as

$$(x, y, z) = T^{-1}(x_p, y_p). \quad (6)$$

However, to remap an image, the inversion expressed in Eq. (6) does not need to be performed explicitly. Instead, a new image grid is defined, for example, along the meridian plane of the test article. In order to remap the PLIF image onto this newly defined image grid, the virtual "image" of each grid cell in the new grid is calculated using Eqs. (3, 4, and 5). The result is a set of four (fractional) pixel coordinates in the original PLIF image (Fig. 13), which may span less than one pixel (Fig. 13a), about one pixel (Fig. 13b), or a number of pixels (Fig. 13c) in the PLIF image (or one or more of the "imaged" corners may lie outside of the boundary of the PLIF image). The remapped PLIF intensity assigned to the pixel in the new grid is now given by a weighted average of pixel values in the original PLIF image. That is,

$$I_{remapped} = \sum_{i,j} I_{original}^{(i,j)} \times F^{(i,j)}, \quad (7)$$

where the summation is over all pixels (i,j) which are inside the imaged regions in Fig. 13, and $F^{(i,j)}$ are the enclosed fractions of the pixels in the original image. It may be noted that the resulting remapped image may have about the same spatial resolution as the original image (as in Figs. 13a and 13b) or less spatial resolution (as in Fig. 13c). Remapping of this sort has been applied to each of the PLIF images and is discussed in Secs. 7.0 and 8.0.

6.0 BACKGROUND SUBTRACTION AND FLAT-FIELD CALIBRATION

Two corrections which were performed on the raw PLIF images before further processing were a dark count subtraction and a flat-field correction. The dark count subtraction is necessary because even in the absence of an optical signal, a nonzero count rate is registered (camera dark count). The dark count rate varies by only a few counts across the image and is assumed to be given by a constant value. This value can easily be determined from an image with the camera lens blocked.

Next, flat-field corrections were performed. This was done by dividing an image (after dark count subtraction) by a flat-field calibration (FFC) image, which is essentially the camera response for a uniform illumination of the ICCD array. Figure 14 shows the FFC image which was used for this purpose. This calibration was performed using a continuous light source and with a rather long gate time on the intensifier array (Ref. 3). Two features stand out. The first is a honeycomb pattern spread over the entire image, characterized by locally reduced sensitivities. This pattern is the result of the hexagonal structure of the intensifier array. The other feature is a more global variation in camera sensitivity across the image. For the FFC file displayed in Fig. 14, this global variation amounts to a variation in sensitivity across the image of about -25 to 25 percent.

Subsequent calibrations of the camera system have shown that the FFC response depends, to some degree, on the mode of operation of the camera. For example, Fig. 15 shows a typical FFC image obtained with a short gate time of 200 nsec and a pulsed laser source. This FFC response is probably more typical for the short gate width operating mode than the FFC response in Fig. 14, which was obtained with a long exposure time and a continuous light source. Analysis of the FFC calibration data is still in progress. In all cases reported here where an FFC was performed, the old calibration from Fig. 14 was used.

Finally, in the PLIF images, there is typically a small background signal, spread roughly uniformly across the image. This background was presumed to be the result of diffuse laser scatter and/or secondary fluorescence emission (reabsorption and reemission of fluorescence radiation outside the PLIF laser sheet). Typically, this background level was determined by calculating the column-averaged signal outside of the laser sheet and performing a linear fit across the image. For example, for the PLIF image for Run 14, a background baseline was found that slopes linearly from 6 counts on the left side of the image to 2 counts on the right. Following dark count subtraction and flat-field correction, such baseline signals were also subtracted from the images.

7.0 PLIF IMAGES FOR RUNS 16 AND 19

7.1 RUN 16

Because they are more easily interpreted, the PLIF images for Runs 16 and 19 are discussed before those of Runs 14 and 15. Figure 16 shows the raw PLIF image obtained for Run 16. The laser sheet was directed along the meridian plane of the test article (see Fig. 2b). Thus there is no PLIF signal below the surface of the model. The edges of the laser sheet are clearly discernible. Figure 17 shows the same image in which the model surface, the model point at 3 in. from the nose, and the schlieren shock position have been projected. This shock position was determined as described in Sec. 3.0. Specifically, the dotted line in Fig. 17 was obtained by projecting the curve-fitted position of the schlieren shock onto the PLIF image. Both the projected model surface and the projected shock match the corresponding features in the PLIF image well. This is convincing proof that the approach to obtaining the geometric scaling between test article and image coordinates through the use of calibration images as described in Sec. 4.0 is sound. In particular, the pre-run scaling transformation could be applied without the need for any fine-tuning, indicating that none of the optics deviated from the pre-run alignment during the Impulse Facility run.

Clearly, the intensity profile of the laser sheet in Figs. 15 and 16 is nonuniform. To correct for this, the average PLIF signal was calculated in the free-stream region in Fig. 16. Essentially, this profile was obtained by column averaging the image in the free-stream region. However, the small divergence of the laser sheet was accounted for (namely, by manually selecting the nonvertical edges of the laser sheet before calculating the average profile). Also, a spline-smoothing algorithm was employed to reduce the noise on the resulting profile, which is shown in Fig. 18. The horizontal scale in Fig. 18 is essentially a pixel scale, but corrected for sheet divergence. The signal outside of the sheet was used for the determination of the background signal.

Following this procedure, the PLIF image was energy-normalized by dividing the PLIF image, roughly column-wise (while accounting for the slight beam divergence), by the net profile in Fig. 18 (that is, after subtracting the sloping base line). Obviously, this normalization is only meaningful where the laser intensity is above the noise level of the image, so that the normalized image has to be truncated at the laser sheet edges (and, of course, the image must be truncated below the model surface, since there is no PLIF signal below the edge of the model).

Finally, after performing the dark count subtraction, the flat-field calibration, the background subtraction, and the energy normalization, the PLIF image was remapped to test article coordinates using the procedure described in Sec. 5.0. The result is shown in Fig. 19. Also shown in Fig. 19 is the edge of the test article and the model point at 3 in. from the nose.

Figure 20 shows average radial profiles of the PLIF signal through the center of Fig. 19 (at an axial position of 83.0 mm), as well as average profiles to the left and to the right of the center. The profiles were obtained by averaging the PLIF signal over 28.5-mm-wide bands, each spanning one-third of the width of the laser sheet. A dimensionless radial coordinate was chosen which is zero at the model surface and one at the shock (as determined from the schlieren image). In this way, averaging over a band of finite width does not cause an appreciable blurring of the shock position.

Extensive discussion of the flow features in Figs. 19 and 20 is given in AIAA paper 94-2621 (Ref. 1). In particular, the comparison between this processed PLIF image and the synthetic PLIF image obtained through Computational Flow Imaging is discussed in Ref. 1. Briefly, there is reasonable agreement between the experimental and theoretical radial profiles around the shock position; both are characterized by an increase in PLIF signal when passing from the free-stream into the shock, followed by a subsequent drop in signal when moving even closer to the model surface. However, whereas the CFD/CFI calculation predicts that the signal should continue to decrease toward the model surface, the experimental signal rises again near the model surface.

This discrepancy has not been resolved and may be explained in several ways: (1) the NO density predicted by the CFD code is too low near the surface; (2) the temperature predicted by the CFD code is too high near the surface; or (3) the experimental PLIF signal close to the model surface contains a laser-induced fluorescence component from an unidentified flow species or an unidentified spectral line of the NO molecule. The latter possibility seems remote, because no other tabulated spectral features could be identified at the excitation wavelength used for Runs 14, 15, and 16 (225.716 nm).

(Following the presentation of Ref. 1, further CFD/CFI simulations have been performed. These indicate that, unlike assumed ad-hoc in Ref. 1, thermal nonequilibrium in the free-stream region is *not* responsible for the decrease in PLIF signal when passing from the free stream into the shock. Thermal nonequilibrium (unequal rotational and vibrational temperatures of the NO absorbers) *does* appear to be present, but does not seem to significantly affect the PLIF signal in the transition between the free stream and the shock. However, attenuation of the laser sheet as it propagates through the free stream was not included in the analysis discussed in Ref. 1 and has now been shown to cause this very decrease in PLIF signal when passing from the free stream into the shock. But, even after incorporating the effect of laser attenuation in the CFD/CFI analysis, the experimentally observed rise in PLIF signal when approaching the model surface is not explained by the CFD/CFI calculations; a more complete analysis will be presented at a later time.)

7.2 RUN 19

To reduce speculation that an accidental spectral coincidence with another species was the reason for the unexplained signal close to the model surface in Run 16, the laser was operated at a different wavelength (225.987 nm) for Runs 17, 18, and 19. Unfortunately, no triggers were received for Runs 17 and 18. The PLIF image resulting for Run 19 is shown in Figs. 21 and 22. Figure 21 shows the raw image; Fig. 22 shows the fully processed image, which may be compared directly with that for Run 16 in Fig. 19.

Population fractions of the laser-excited state in NO, absorption cross sections, and fluorescence yields should be roughly similar for the 225.987-nm transition and that used for the other PLIF images (225.716 nm). This is shown in Fig. 23, which shows the temperature dependence of the PLIF signals at the two wavelengths assuming equal NO number densities (the quantity plotted in Fig. 23 is the product of the NO population fraction and the Einstein B coefficient for the respective transitions, assuming equal rotational and vibrational temperatures). Also, the average laser pulse energies were comparable for the two images. In fact, the camera had been moved closer to the tunnel window, which should have resulted in a gain in signal of about a factor 2.5 for Run 19 compared with Run 16. Nevertheless, the signal level (and hence the signal-to-noise ratio) for Run 19 is much lower than that for Run 16, for unknown reasons.

Still it appears that the character of the image for Run 19 is very similar to that for Run 16. In particular, a dark band can be seen to run through the images in Fig. 22, much like the one which runs through the processed PLIF image in Fig. 19. There is also a somewhat smaller dark band just above the model surface, immediately to the right of the model joint.

Figure 24 shows average radial profiles at the center of the PLIF image from Fig. 22 (at an axial location of 76.5 mm), as well as average profiles to the left and to the right of the center. These profiles were obtained in similar fashion to those shown for Run 16 in Fig. 20, namely by averaging over three vertical regions, each with a width equal to one-third the width of the laser sheet (28.1 mm). The shapes of the profiles in Fig. 24 are quite similar to those in Fig. 22. The main difference is that the ratio between the peak signal inside the shock and the free-stream value signal is smaller (about 1.4) than it is for Run 16 (about 2.2). This trend is consistent with the different temperature-dependences of the two transitions shown in Fig. 23. For a more thorough quantitative check, a CFD solution for Run 19 would be required.

8.0 PLIF IMAGES FOR RUNS 14 AND 15

8.1 RUN 14

PLIF images were obtained for Runs 14 and 15. In both cases, the laser sheet was aligned so as to pass in front of the model surface without being intercepted by the test article (see Fig. 3a). This alignment was performed so that the laser sheet was parallel to the model surface and separated from it by about 5 mm. However, it appears that, for both Run 14 and Run 15, the laser sheet moved during the Impulse Facility run, as argued below.

Figure 25 shows the raw PLIF image for Run 14. The overall signal level is rather low. Some natural flow emission is observed on the left side of the image, just downstream from the nose cone. Also, with proper pseudo-color rendering, an even smaller level of background emission can be discerned on the far right-hand side, along the edges of the test article.

Figure 26 shows the average horizontal intensity profile obtained from Fig. 25. This profile was obtained by column averaging over the entire height of the signal. Based on Fig. 26 a linearly sloping baseline was assigned for the background signal (shown as the dashed line in Fig. 26), and the raw image was normalized by subtracting this linearly sloping baseline and dividing the resulting image by the average profile of Fig. 25. The resulting energy-normalized image is shown in Fig. 27.

Several observations are noteworthy. First, although the shape of the high-intensity signal region appears to be roughly symmetric around the centerline, the magnitude of the signal is not. In particular, the average signal in the bottom half of the image is only about 60 percent of that in the top half. This can also be seen in Fig. 28, which shows the average vertical profile, obtained simply by row averaging across the whole width of the energy-normalized image shown in Fig. 27. The observed asymmetry is consistent with the hypothesis that the laser sheet is being attenuated as a result of absorption by NO. Work is in progress to estimate the NO number density on the basis of this observed attenuation.

The second observation is that the vertical extent of the high-intensity signal region in Figs. 25 and 27 is not consistent with the expected size of this region based on the original alignment of the laser sheet. To illustrate this, Fig. 29 shows the projected edges of the test article (as they would have been seen by the camera), the outline of the shock (as determined from the schlieren image for Shot 14), and, most importantly, the projection of the intersection of the laser sheet with the shock. This projection was calculated by assuming that the shock is axially symmetric and that the laser sheet was in the original alignment position (parallel to the model surface at a distance of 5 mm).

On the basis of the PLIF images from Runs 16 and 19, it would be expected that the intersection of the laser sheet with the shock would show up clearly in the PLIF image (Figs. 19 and 22). However, the height of the predicted intersection in Fig. 29 is clearly much taller than the height of the high-signal region in Figs. 25 and 27. The most plausible assumption for this discrepancy appears to be that the laser sheet moved from its original alignment position during the Impulse Facility firing.

To test this assumption, the intersections of the laser sheet and the shock were calculated for a number of sheet positions. For example, Fig. 29 shows the intersections for a series of separations " d " (measured radially) between the laser sheet and the model surface, while keeping the sheet parallel to the surface (the intersection marked by a solid line in Fig. 29 corresponds approximately to the one which would have resulted for the original alignment of the laser sheet). To establish the optimum fit of the observed intersection to the measured intersection, a least-squares fit was performed on hand-picked points from the PLIF image, selected along the top and bottom edges of the high-signal region in the PLIF image. These points, along with the fitted intersection, are shown as overlays on the normalized PLIF image in Fig. 30. The laser sheet position which corresponds to this least-squares fit result is shown in Fig. 31, along with the model surface, the shock, and the original position of the laser sheet. Note that this sheet position has moved considerably farther away from the model surface, and is no longer parallel to the surface.

Having established, in this manner, the actual position of the laser sheet, it was possible to remap the PLIF image to a meridian plane through the test article. The result is shown in Fig. 32, both for the top half of the PLIF image (Fig. 32a) and for the bottom half (Fig. 32b; the signal in this image was divided by 0.6 to compensate approximately for the lower signal as a result of attenuation of the laser sheet). Also shown in Fig. 32 are the predicted positions of the shock, the outline of the model surface, and the vertical point in the test article (Figs. 19 and 22).

A notable difference between Figs. 32 and 22 is that the ratio between the PLIF signal inside the shock to that in the free stream is much larger for Run 14 than for Run 16, where it is approximately 2.2. Because of the extremely low-signal level in the low-intensity region (presumed to be free stream) for Figs. 27 and 32, an accurate value of the "free-stream" fluorescence cannot be obtained. However, the ratio is certainly much larger than 2.2. Based on Fig. 28, this ratio is estimated to be about 20 (± 5). No good explanation is presently available for this difference.

8.2 RUN 15

The results for Run 15 are very similar, except that a much stronger signal was measured. Figure 33 shows the raw PLIF image. Again, there is a high-intensity region with a shape

inconsistent with the expected intersection of the laser sheet and the shock. More structure is evident in Fig. 33 than in Figs. 25 and 27. Also, as in Fig. 25, the signal level in the bottom part of the figure is lower than that in the top part, leading again to the hypothesis that laser attenuation was present as a result of absorption by NO.

Figure 34 shows the average horizontal profile (obtained by averaging across the entire height of the image), and Fig. 35 shows the energy-normalized image, calculated from Figs. 33 and 34. Figure 36 shows the average vertical profile obtained from the normalized image, showing again a ratio of about 0.6 between the PLIF signal below and above the centerline in the PLIF image. As was the case for Run 14, there is a large increase in signal when going from the low-signal region to the high-signal region. From Fig. 36, this ratio is calculated to be $22 (\pm 2)$, consistent with the value found for Run 14.

The same procedure outlined for Run 14 was followed to calculate the actual position of the laser sheet. That is, a set of points was selected in the normalized image which were assumed to define the intersection of the laser sheet with the shock. These points were provided as input to a least-squares fitting program to optimize the laser sheet position. Also included in this fit was the camera pitch angle, δ , (Fig. 9), because it appeared that the camera got bumped slightly from its original alignment position (as witnessed by a vertical shift of the symmetry line of the PLIF image relative to the pre-run calibration image of the test article).

Figure 37 shows two sets of hand-picked points which were used as input to the least-squares fitting program. Also shown are the optimized intersections of the laser sheet with the shock for each set of points. Figure 38 shows the result for the calculated laser sheet positions for both sets of points. Clearly, the calculated positions of the laser sheet depend on how the points representing the intersection between the laser sheet and the shock are selected. That is, how is the position of the edges defined in the vertical profile of Fig. 36? However, it again appears that the laser sheet moved significantly from the original pre-run position. Moreover, the calculated motion of the laser sheet for Run 15 is almost identical to the calculated motion for Shot 14.

Figure 39 shows the result of remapping the normalized PLIF image to a meridian plane through the test article (Fig. 32). The top (a) and bottom portions (b) are shown separately. Finally, Fig. 40 shows an enlargement (calculated separately) of the detail region marked in Fig. 39b. This is the region that contains the remapped diagonal "streak" which is clearly seen in the left bottom corner of the raw PLIF image from Fig. 33 (a less prominent streak at a different angle is also visible in the top left region of the image). This streak is likely the result of some flow disturbance (perhaps as a result of a temporary deposit of particulate matter on the nose tip; deposits have been observed after a run). As a result of the remapping transformation, the angle of this streak is aligned much more closely with a streamline than might be expected from the roughly 45-deg angle in the raw PLIF image.

9.0 DISCUSSION AND SUMMARY

The number of PLIF images obtained during FY94 runs of the Impulse Facility was smaller than anticipated. One consequence of this was that no images were obtained for identical operating conditions of the facility. Nevertheless, the four images which were obtained constitute a sufficient database to allow a detailed comparison with CFD predictions. So far, such a detailed comparison has only been performed for the PLIF image from Run 16. Although incomplete (for example, the effect of laser attenuation was not included in the analysis which was presented in AIAA paper 94-2621), it has pointed out some significant discrepancies between the measured and calculated data. Quite possibly, these discrepancies point at inadequacies of the CFD model. However, it would be desirable to perform further experimental testing to eliminate the possibility that systematic errors are introduced in the measurement process and the PLIF data analysis. Specific experiments had, in fact, been planned, but had to be forfeited when the number of Impulse Facility runs was curtailed from the original plan.

In addition to significantly expanding the database for the Impulse Facility, the present effort has resulted in a clear understanding of the process which is required to acquire quantitative PLIF images in a complex facility. This includes the use and analysis of calibration images that are required for proper scaling of the images. For example, perfect agreement was found between measured locations of the bow shock determined independently by PLIF and by schlieren imaging for Run 16.

No such agreement could be established for Runs 14 and 15, presumably as a result of motion of the laser sheet during the Impulse Facility runs. Clearly, such motion is undesirable and should be avoided in future tests by firmly securing the laser sheet optics (as was done following Run 15). However, with the aid of the PLIF analysis techniques developed during this effort, it was possible to reconstruct the likely laser sheet positions based on the measured schlieren shock positions.

Still it would be of great interest to repeat the setup used for Runs 14 and 15 (laser sheet passing in front of the test article), because the behavior of the PLIF signal is dramatically different from that in Runs 16 and 19 (with the laser sheet along a meridian plane of the test article). By securing the laser sheet optics securely there should be no need for a posttest optimization of the laser sheet position. An analogous geometry of interest would be one in which the laser sheet is positioned nearly perpendicular to the test article, so that the intersection of the laser sheet with the shock would appear as a crescent arc.

Having successfully developed a procedure for acquiring, calibrating, and processing of PLIF images in the Impulse Facility, the emphasis of future work should be directed in particular to

resolving the discrepancies between the PLIF images and the computational results. The recommended approach for this is to select a particular operating condition for the Impulse Facility, and acquire a set of PLIF images for different laser sheet geometries and different excitation wavelengths (perhaps simultaneously using a dual PLIF setup). Along with this experimental work there should be a computational effort to resolve such questions as to why the predicted nitric oxide density near the model surface might be too low or why the predicted temperature in this region might be too high. The combined effort should lead to a stronger confidence in the accuracy of the computational results and might lead to significant improvements in modeling the complex kinetics of high enthalpy flows.

REFERENCES

1. W. M. Ruyten, W. D. Williams, and F. L. Heltsley. "Computational Flow Imaging for Planar Laser Induced Fluorescence Applications." AIAA Paper 94-2621, 18th AIAA Aerospace Ground Testing Conference, Colorado Springs, CO, June 20-23, 1994.
2. M. S. Smith, W. D. Williams, L. L. Price, and J. H. Jones. "Shocktube Planar Laser Induced Fluorescence Measurements in Support of the AEDC Impulse Facility." AIAA Paper 94-2649, 18th AIAA Aerospace Ground Testing Conference, Colorado Springs, CO, June 20-23, 1994.
3. J. T. Tarvin. "Characterization of an Intensified Charge-Coupled Device (ICCD) Camera Used in Planar Laser-Induced Fluorescence (PLIF) Studies." USAF Summer Faculty Research Program 1993, Final Report, Vol. 6, p. 7, Research and Development Laboratories, Culver City, CA, 1993.

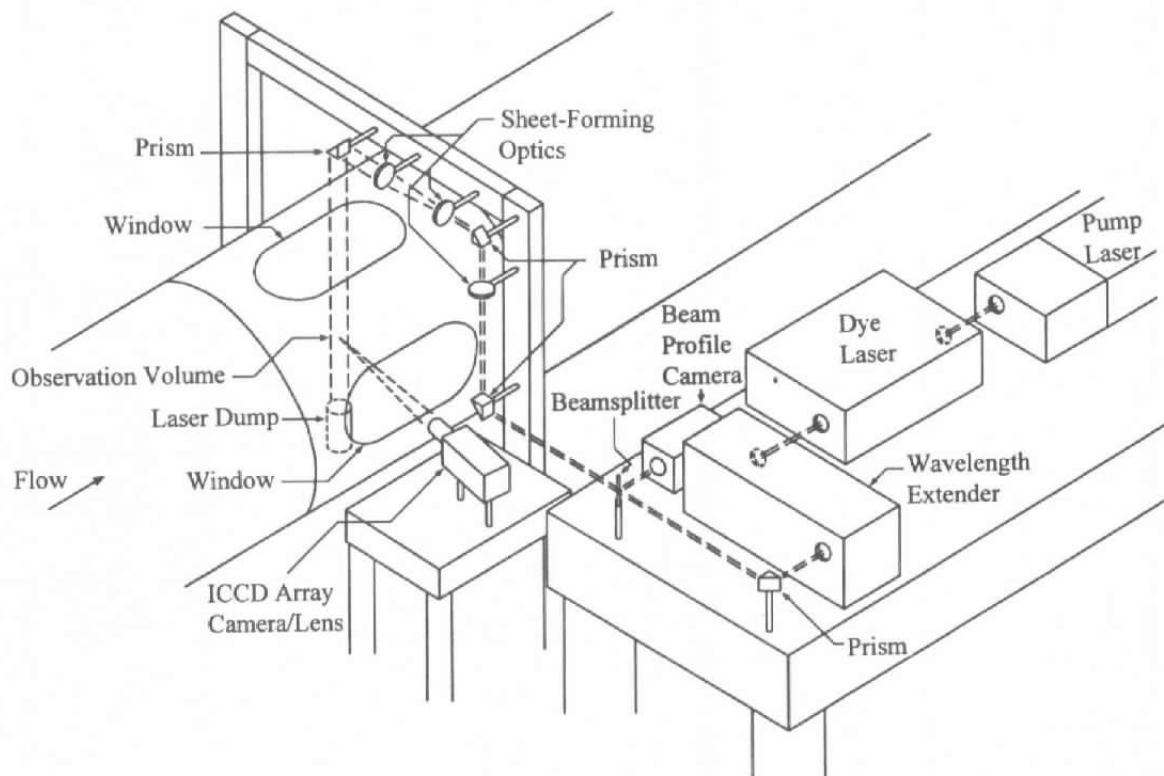
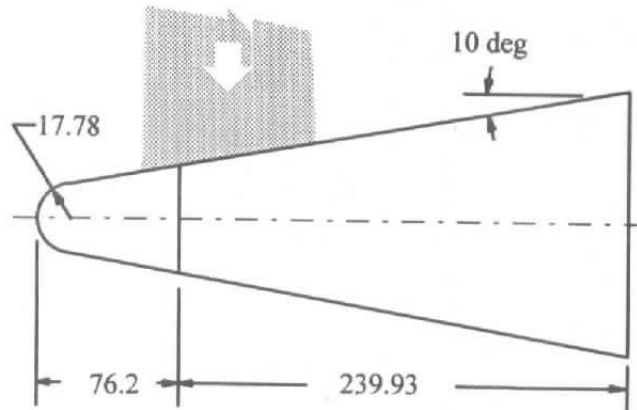


Figure 1. PLIF experimental setup at Impulse Facility.



Dimensions in mm

Figure 2. Schematic of test article.

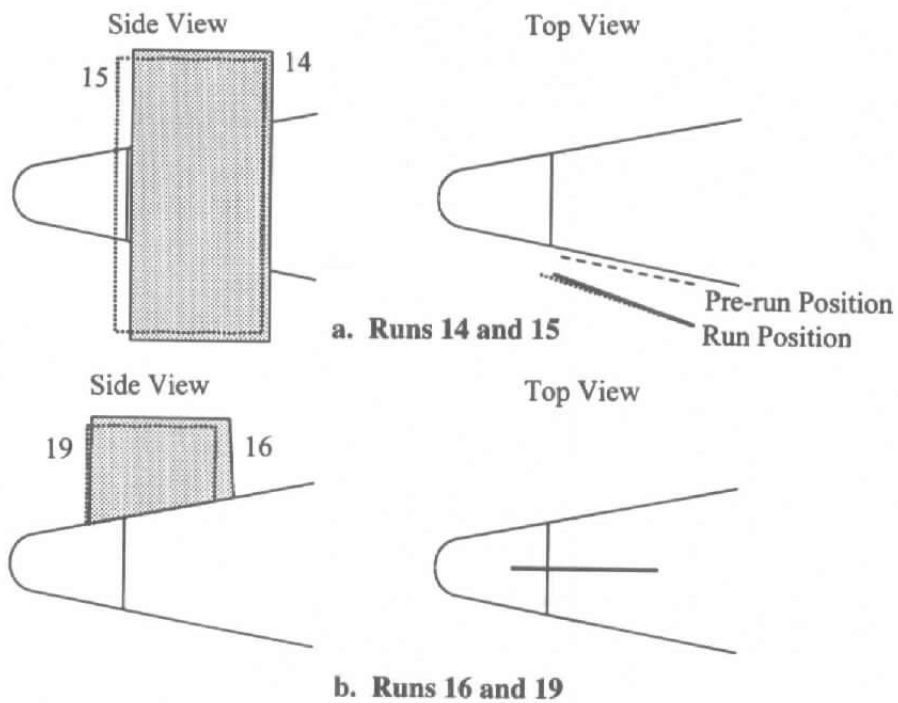


Figure 3. Laser sheet geometries relative to test article.

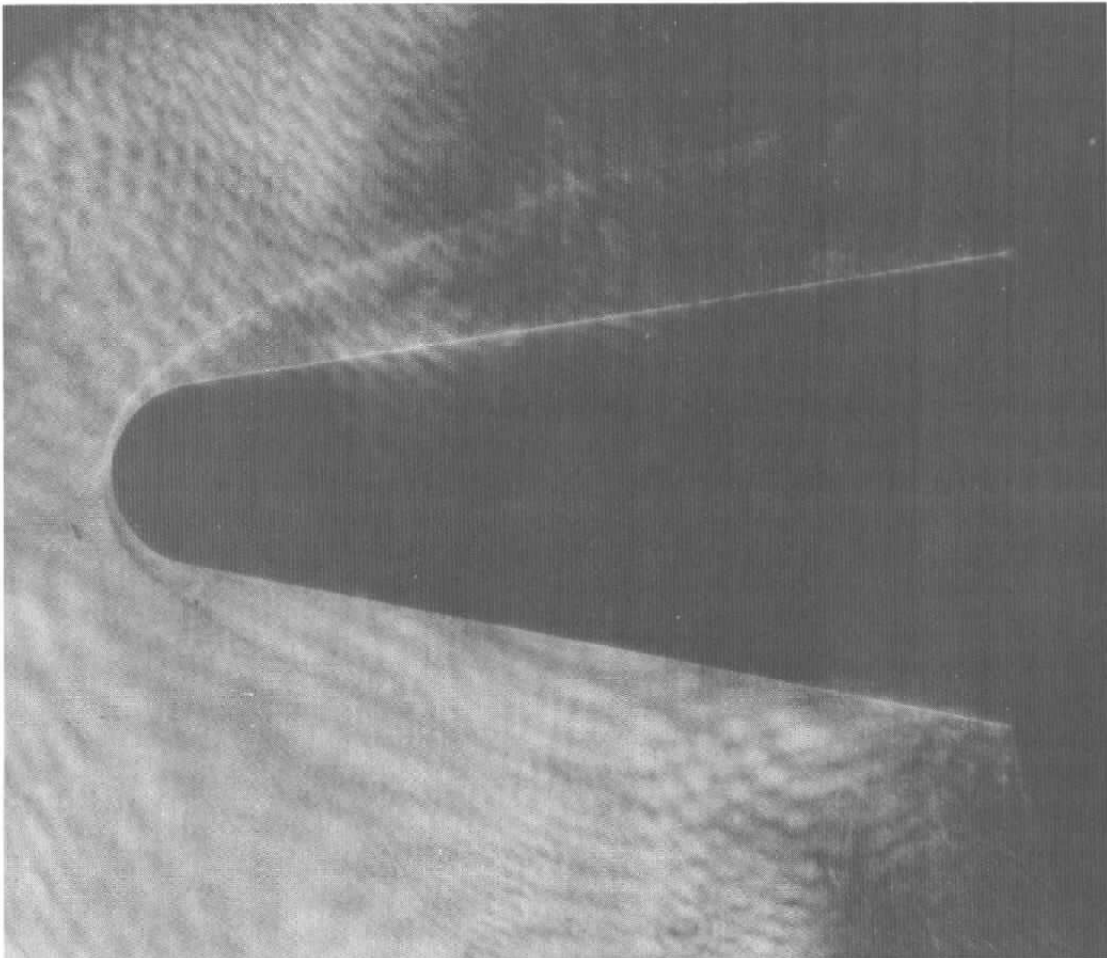


Figure 4. Schlieren image for Run 16.

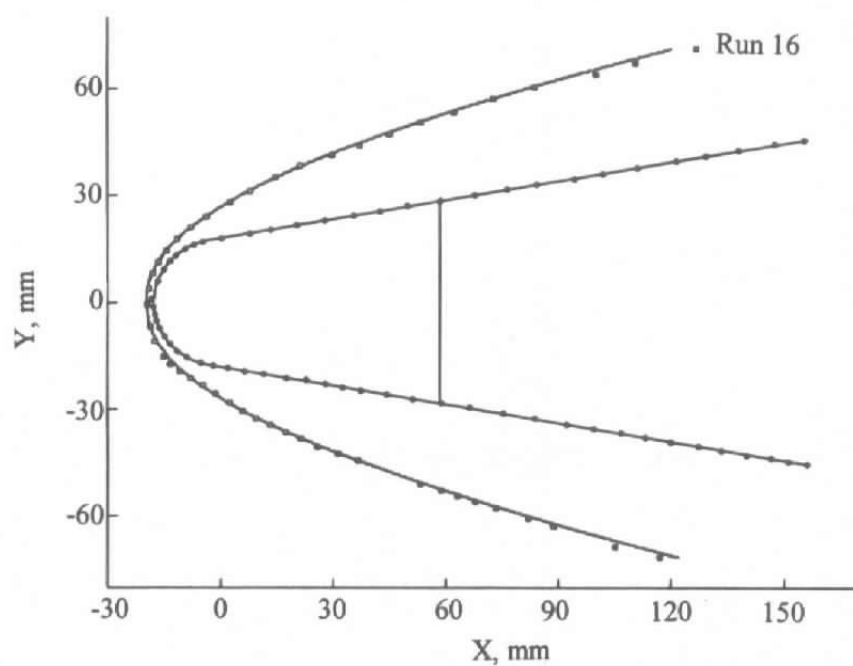


Figure 5. Result of digitizing and fitting of schlieren shock position for Run 16.

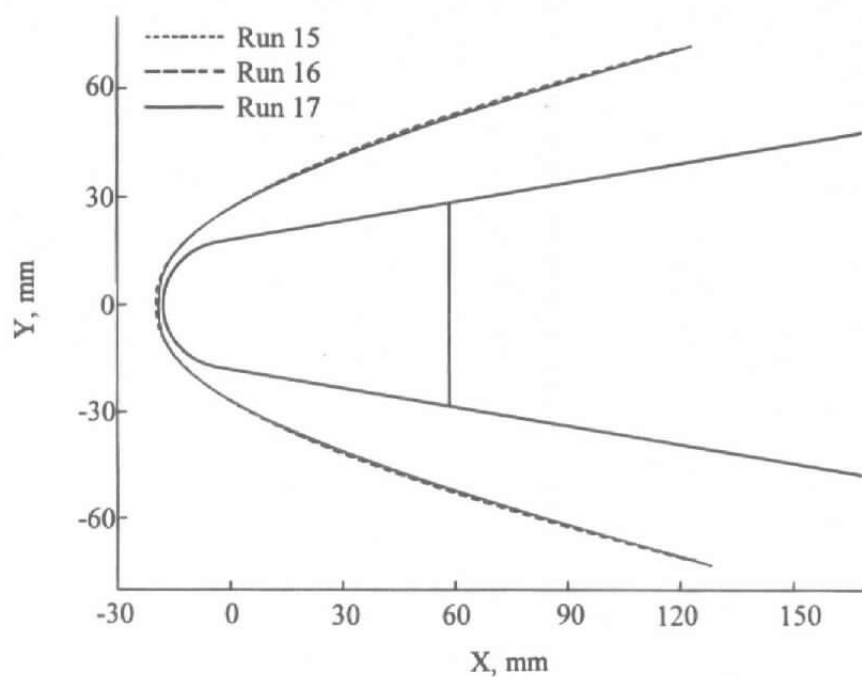


Figure 6. Fitted schlieren shock positions for Runs 14, 15, and 16.

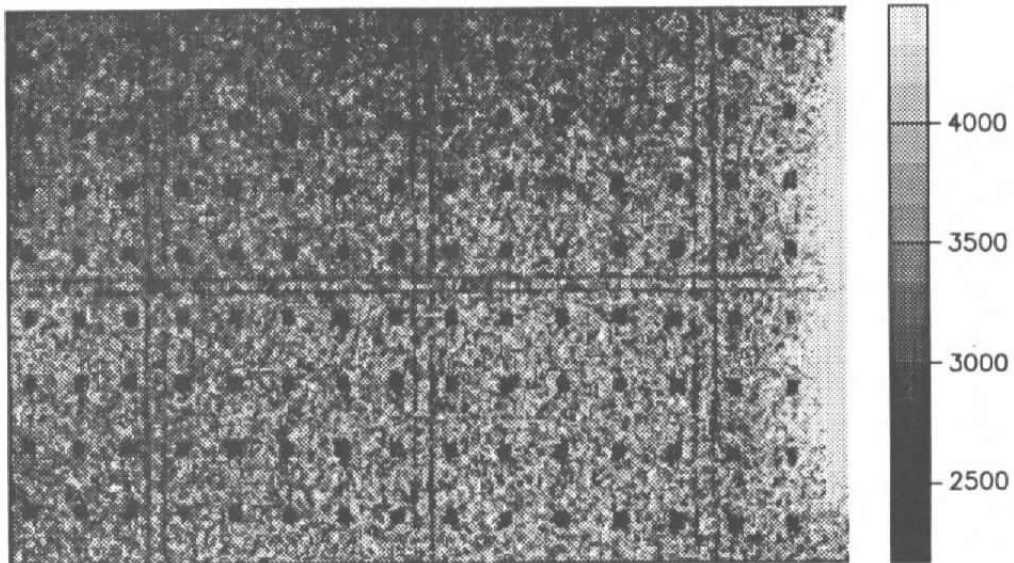


Figure 7. Image of calibration target used for Run 15.

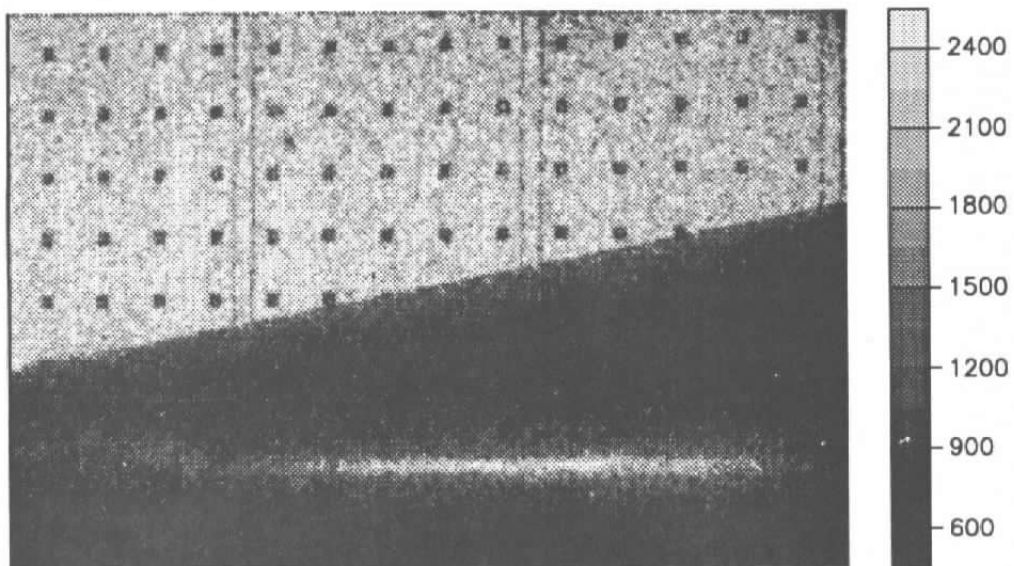


Figure 8. Image of calibration target used for Run 16.

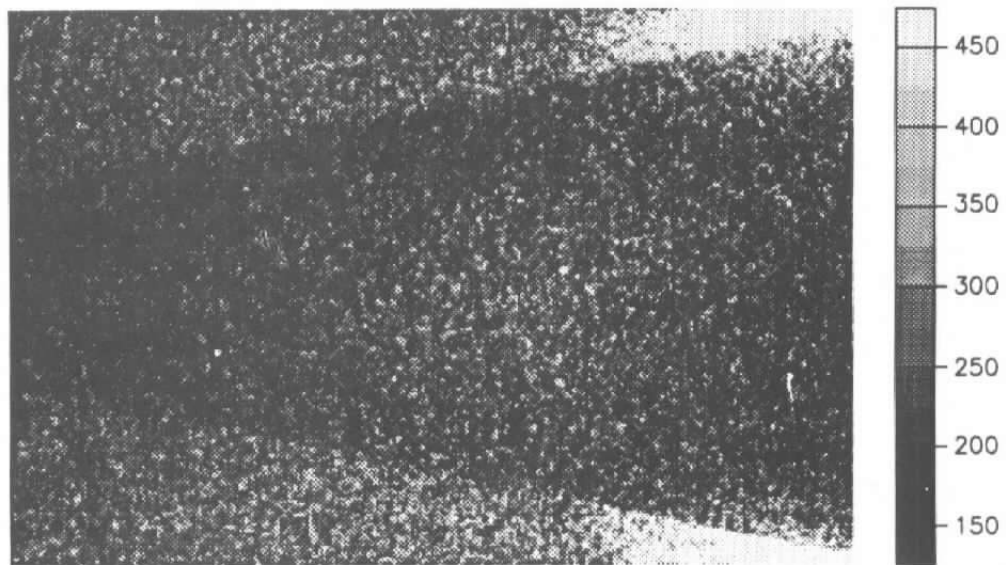


Figure 9. Back-lit image of the test article for Run 15.

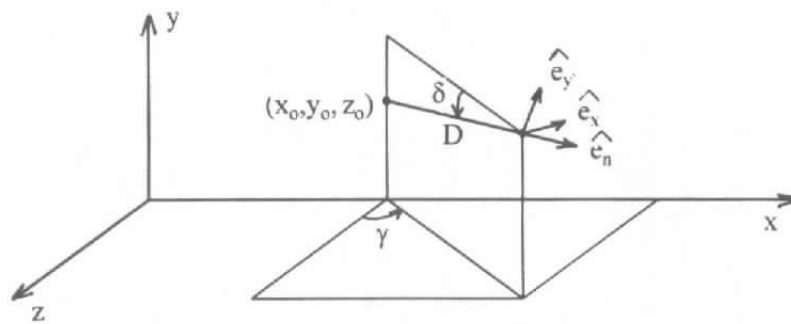


Figure 10. Definition of camera orientation relative to test article coordinate system.

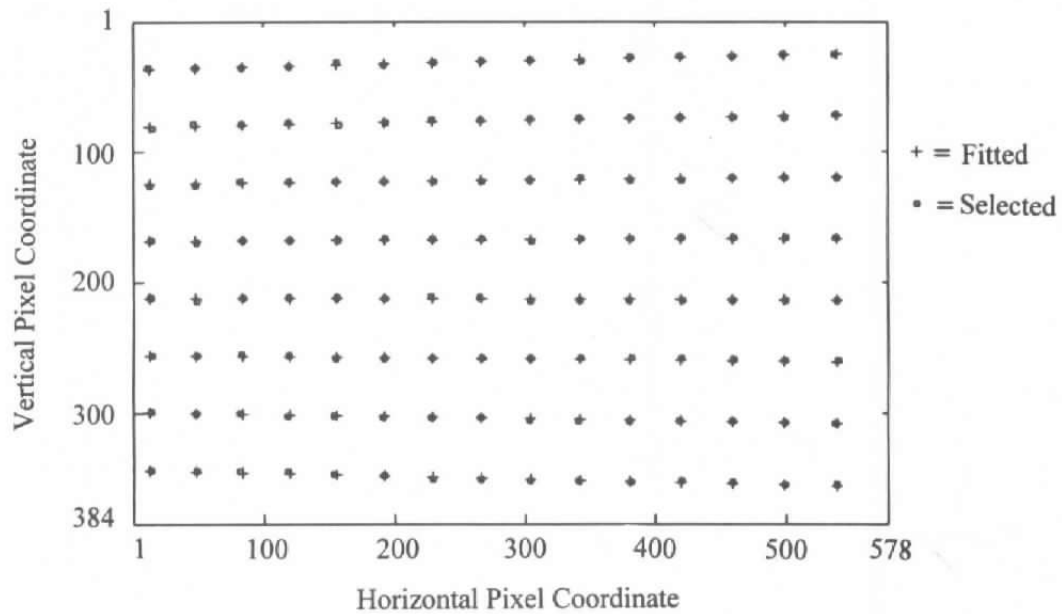


Figure 11. Comparison of selected and fitted marks for calibration image from Fig. 7.

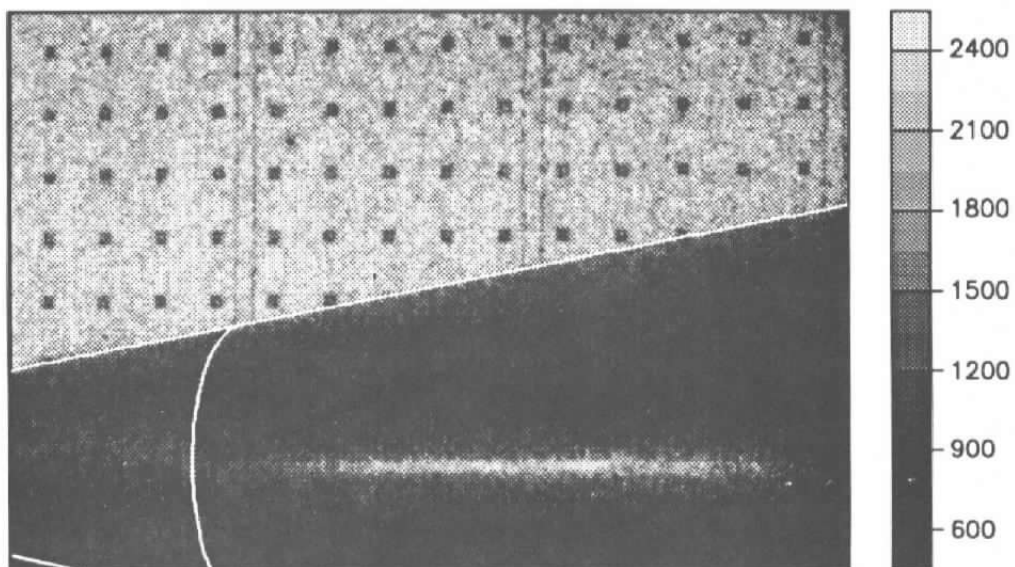


Figure 12. Overlay of fitted test article features on calibration image from Fig. 8.

Remapped Grid Original Grid

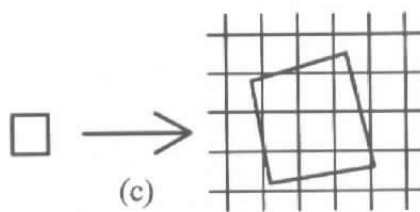
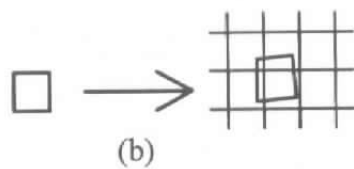
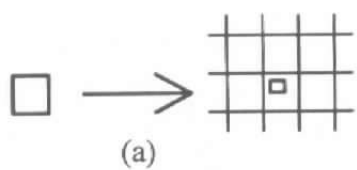


Figure 13. Examples of projections of remapped image pixel onto original image grid.

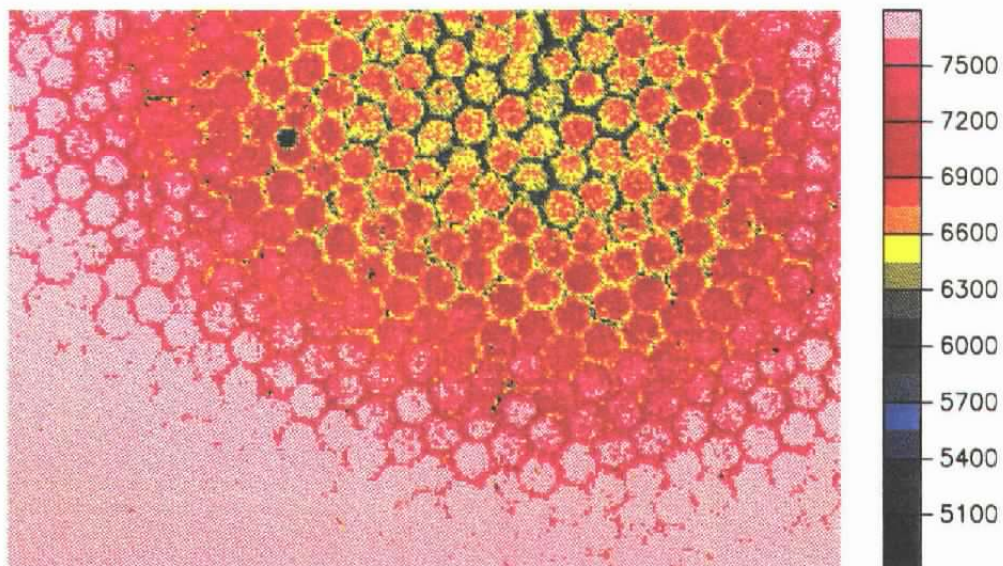


Figure 14. Flat-field calibration image obtained with continuous light source and long gate.

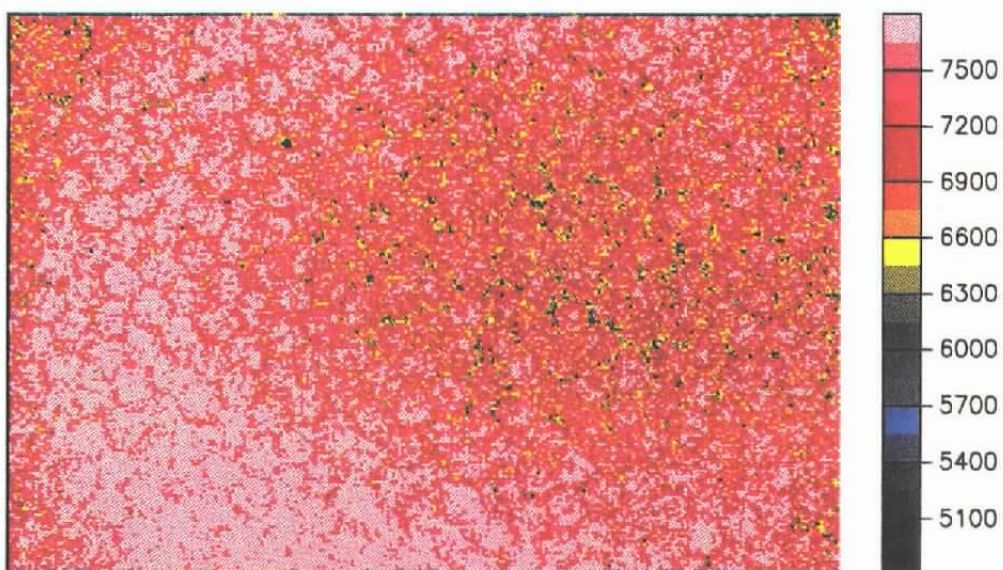


Figure 15. Typical flat-field calibration image obtained with a short laser pulse and a short gate.

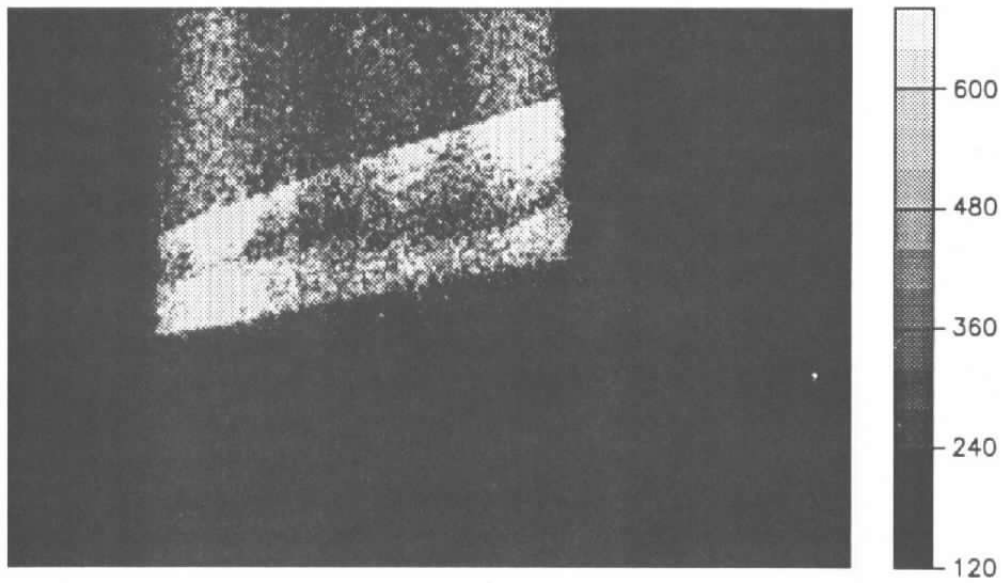


Figure 16 . Raw PLIF image for Run 16.

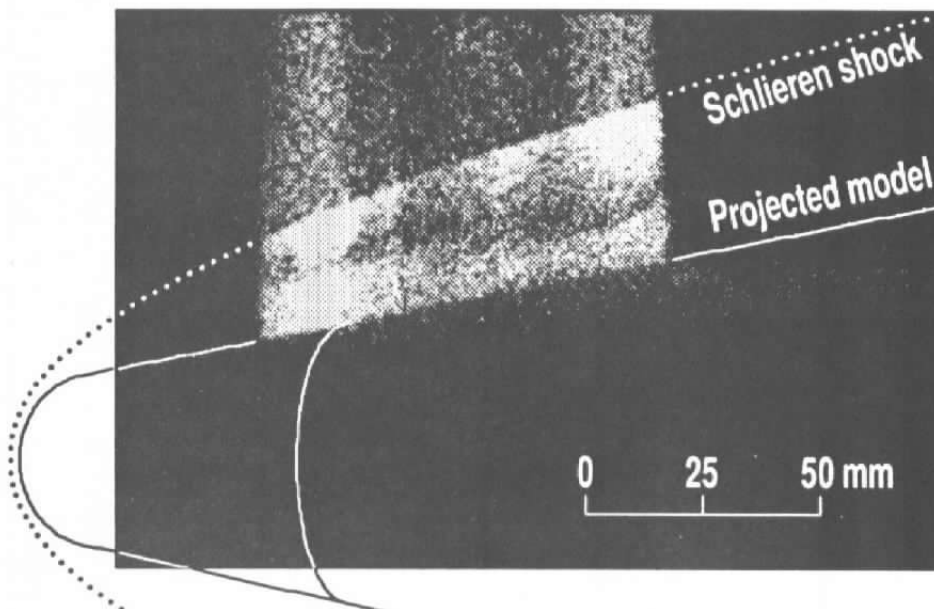


Figure 17. Run 16 PLIF image overlaid with projection of model and shock.

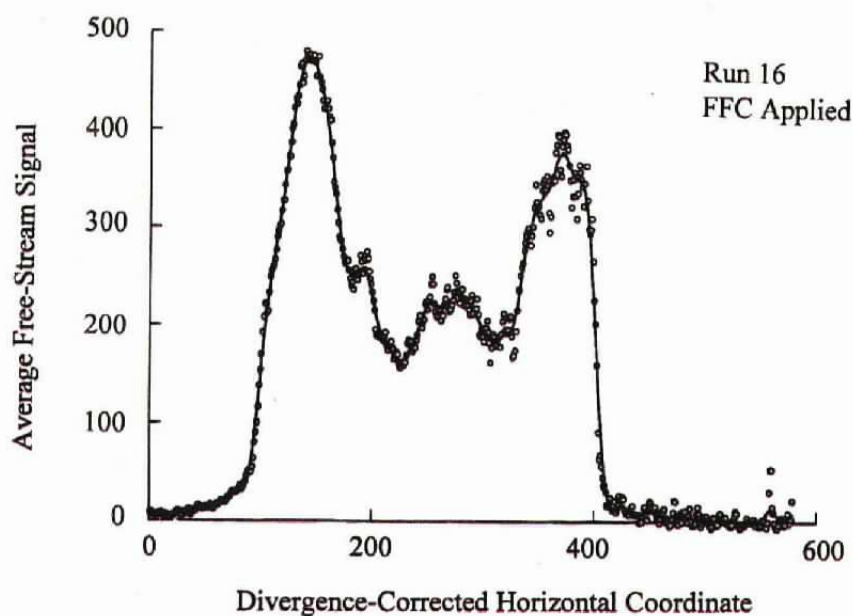


Figure 18. Average horizontal profile of free-stream region in Fig. 16.

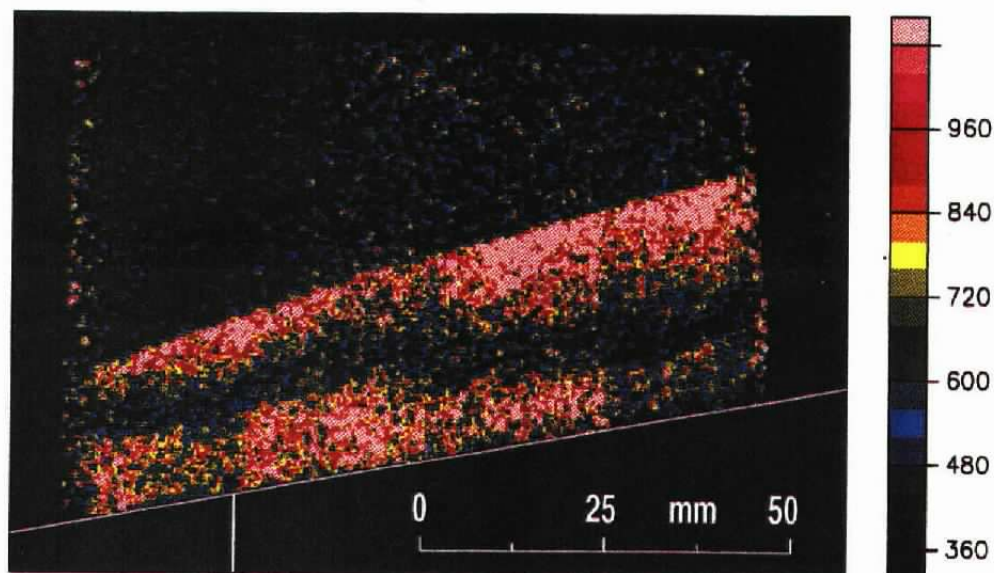


Figure 19. Remapped, energy-normalized PLIF image for Run 16.

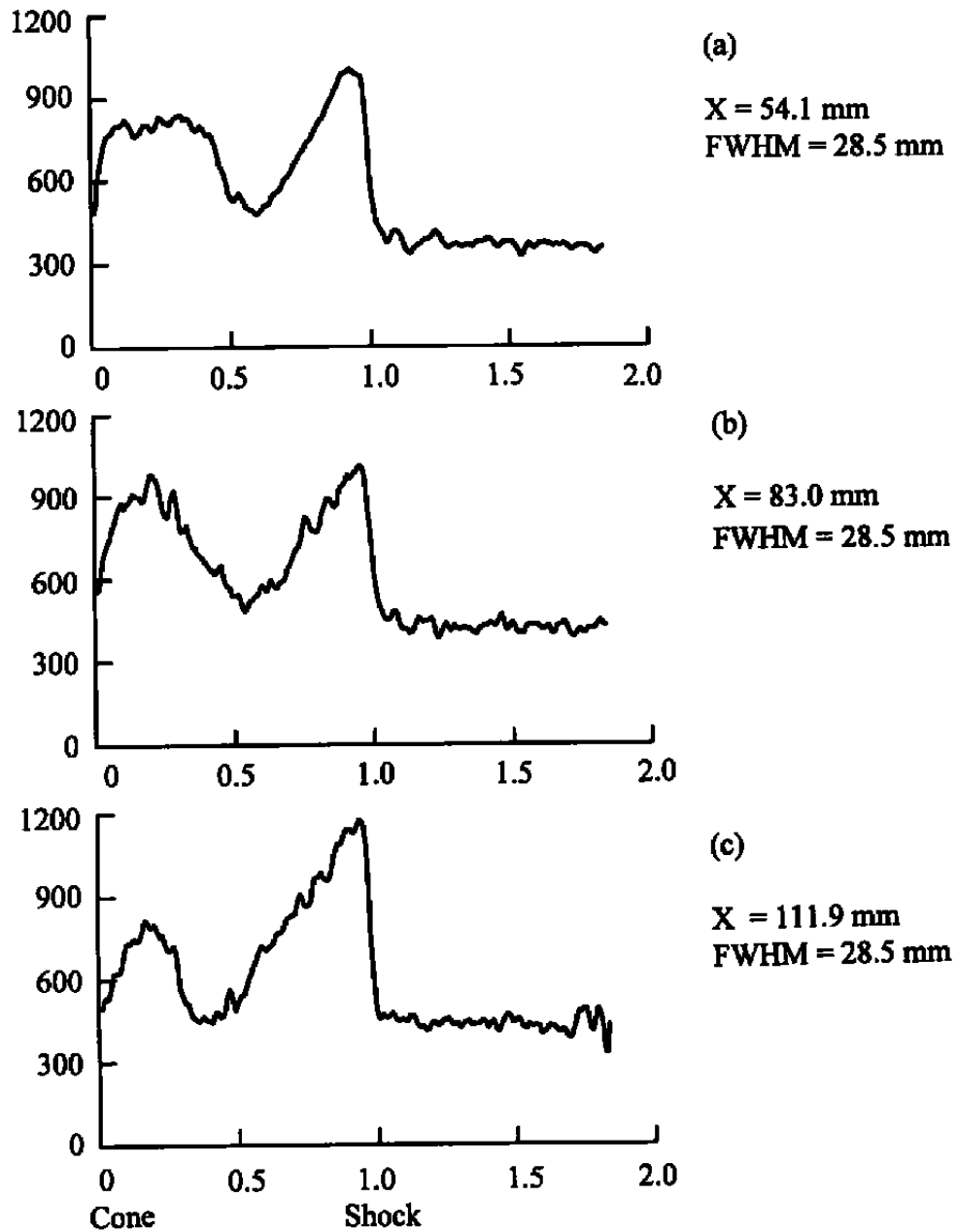


Figure 20. Average radial PLIF profiles through the center of Fig. 19.

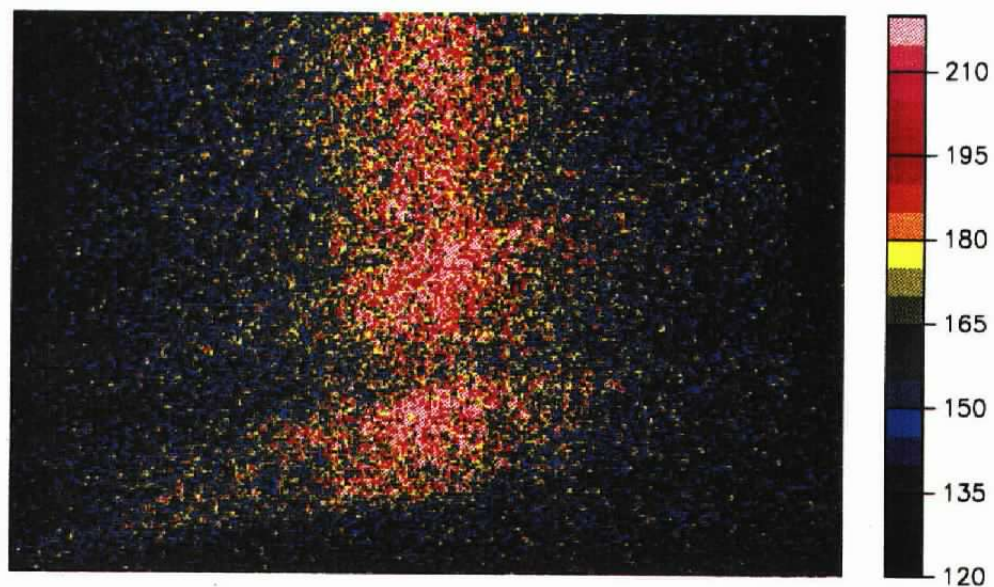


Figure 21. Raw PLIF image for Run 19.

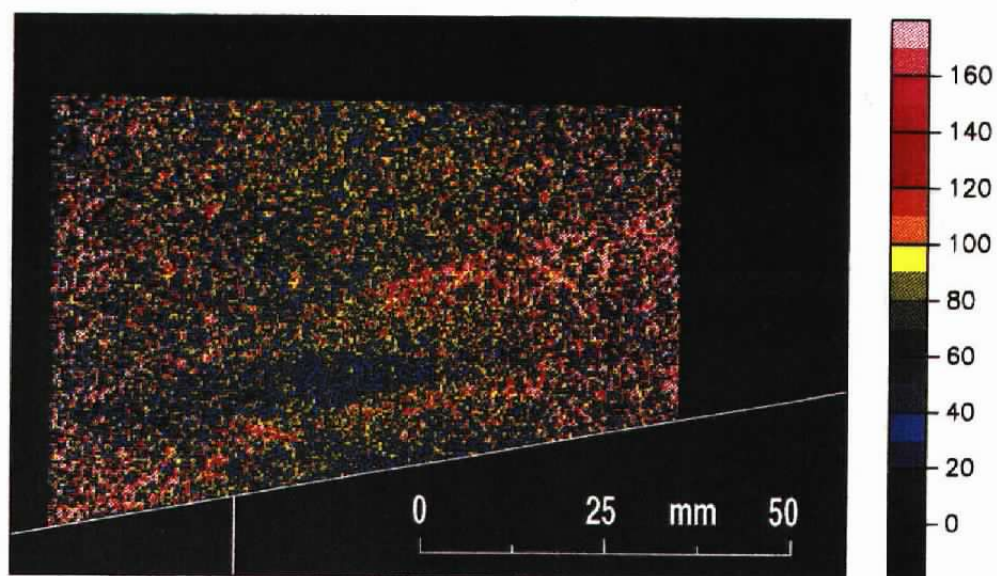


Figure 22. Remapped, energy-normalized PLIF image for Run 19.

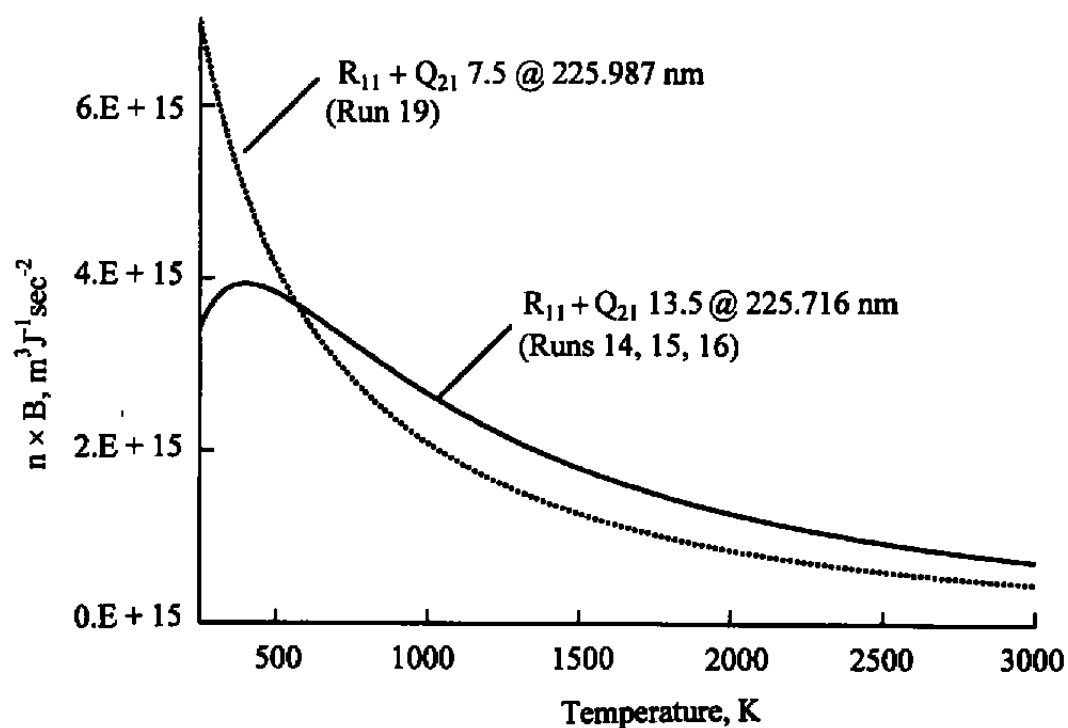


Figure 23. Temperature dependence of the PLIF signal for the two transitions used in this work.

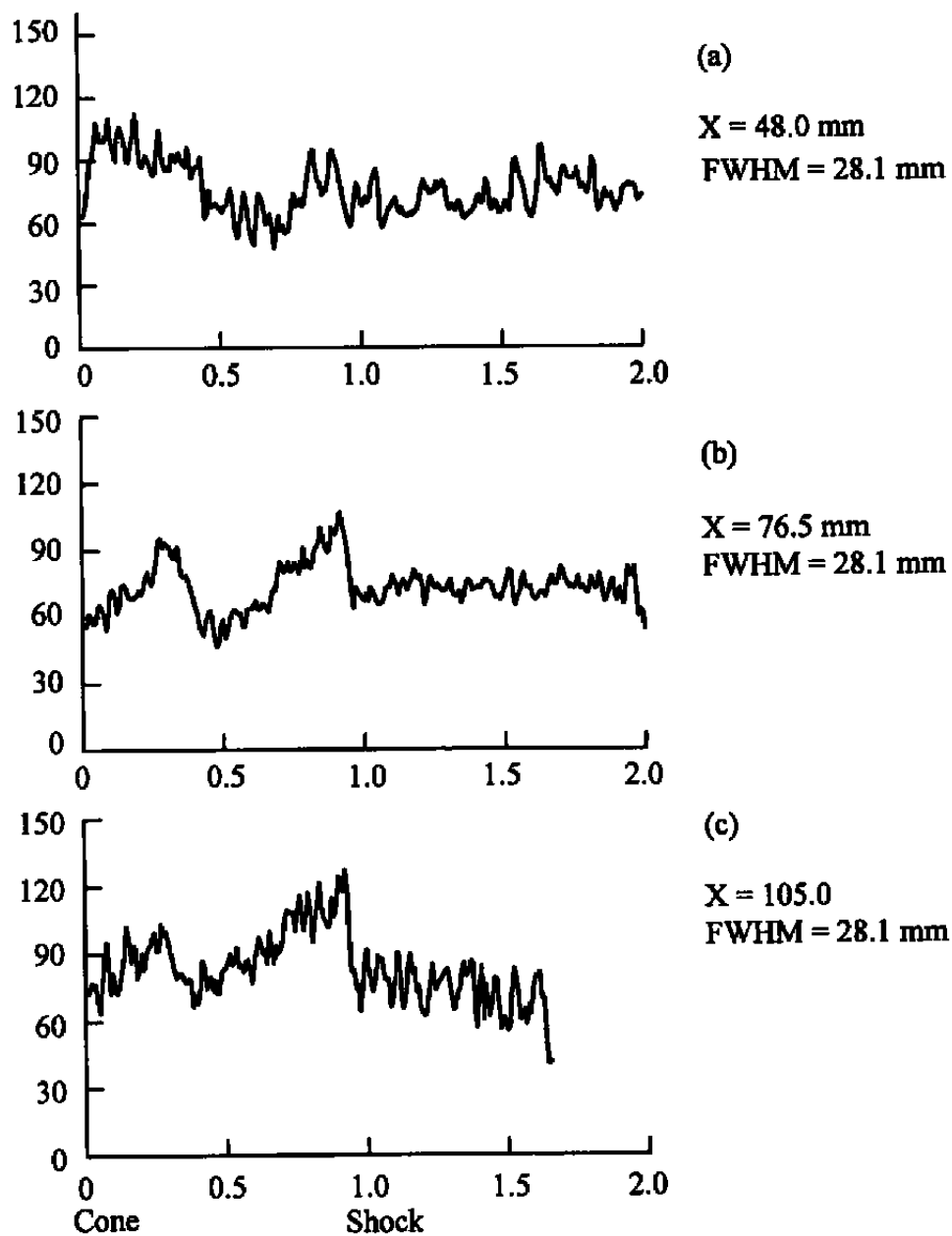


Figure 24. Average radial PLIF profiles through the center of Fig. 22.

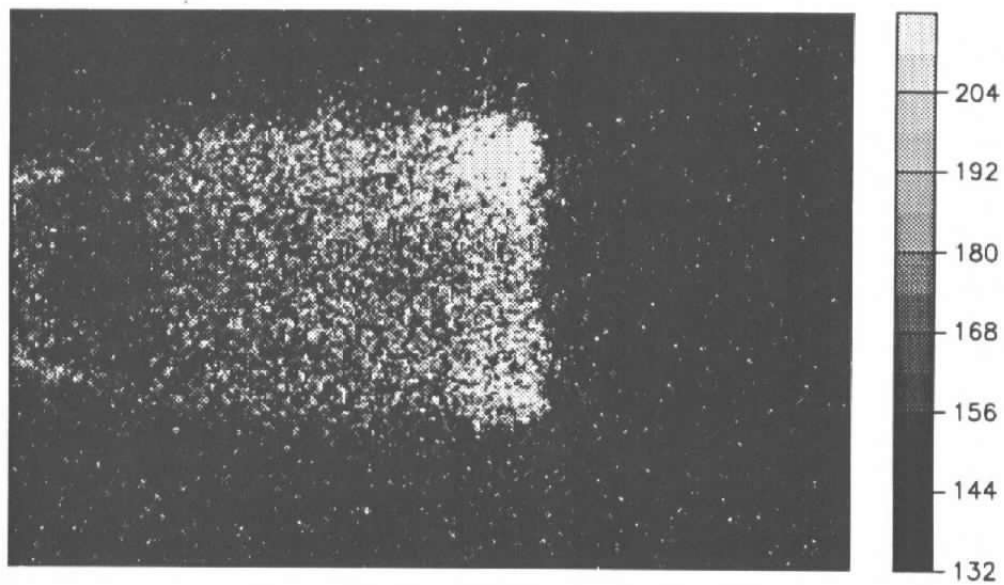


Figure 25. Raw PLIF image for Run 14.

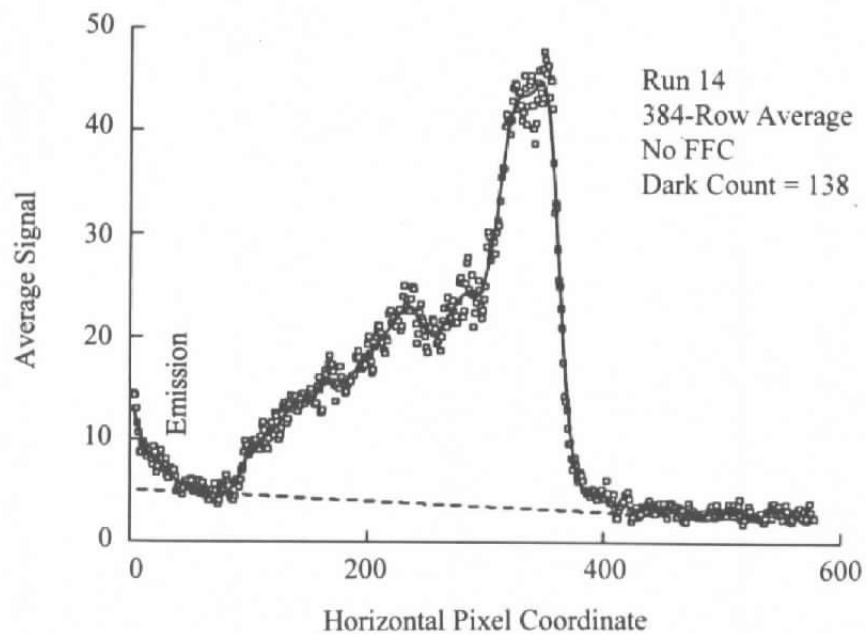


Figure 26. Average horizontal profile of the raw image from Fig. 25.



Figure 27. Energy-normalized PLIF image for Run 14.

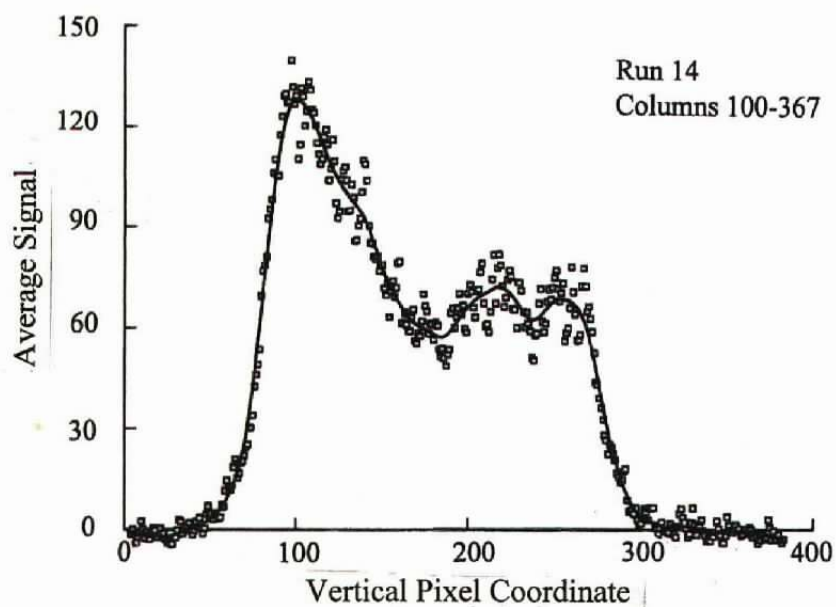


Figure 28. Average vertical profile of the PLIF signal in Fig. 27.

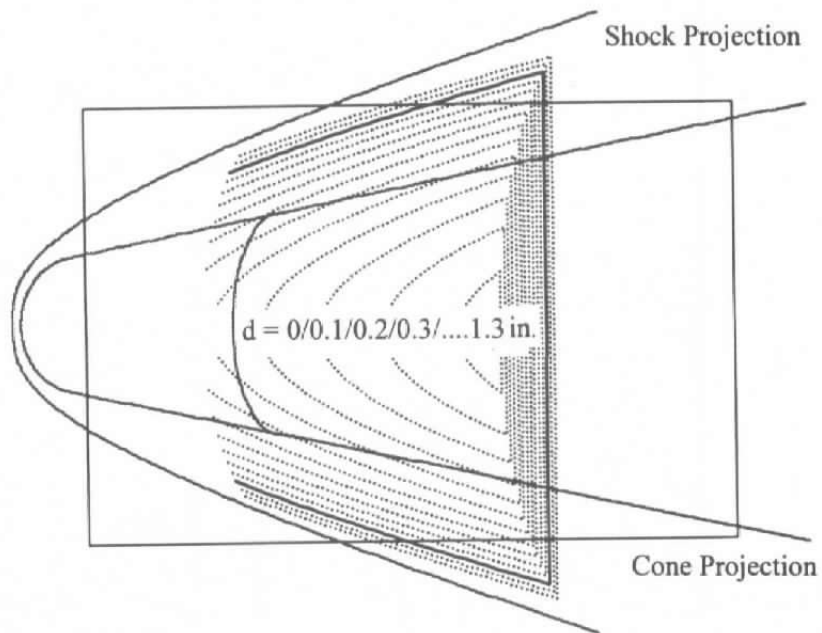


Figure 29. Expected projections of the intersection of the laser sheet with the shock, as seen by the camera for Run 14, for various distances between laser sheet and edge of the model.

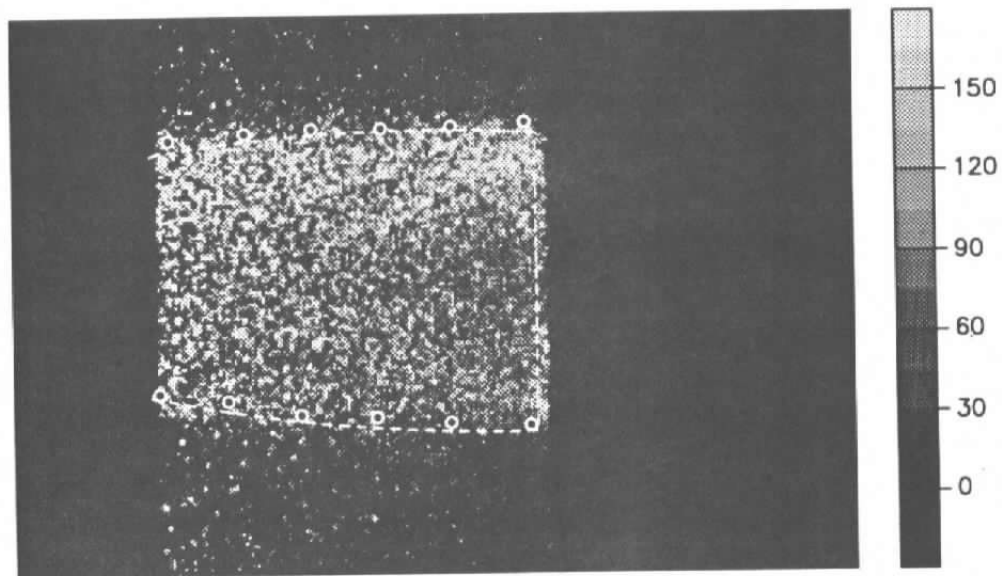


Figure 30. Overlay of selected and fitted intersection points between laser sheet and shock on energy-normalized PLIF image from Fig. 27.

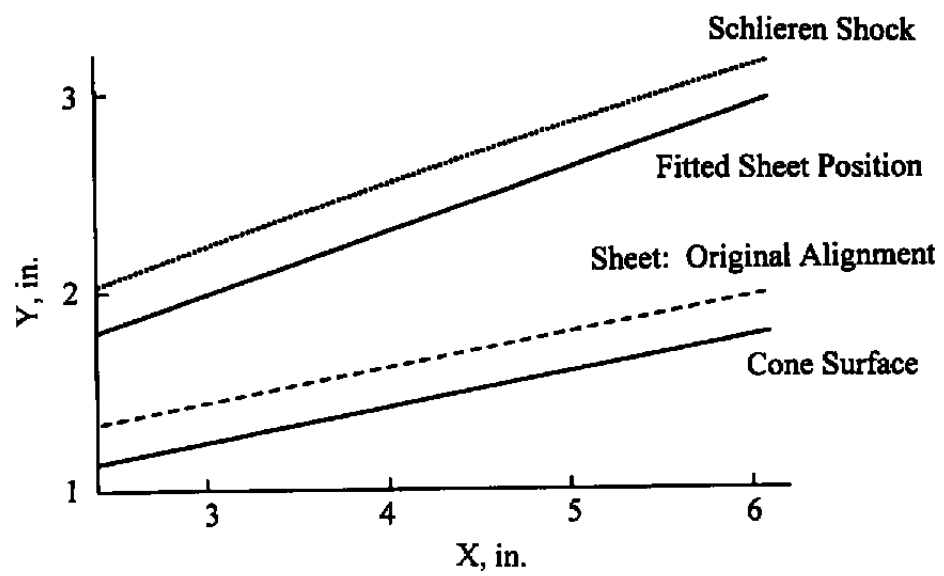


Figure 31. Fitter laser sheet position for Run 14 shown in test article coordinates.

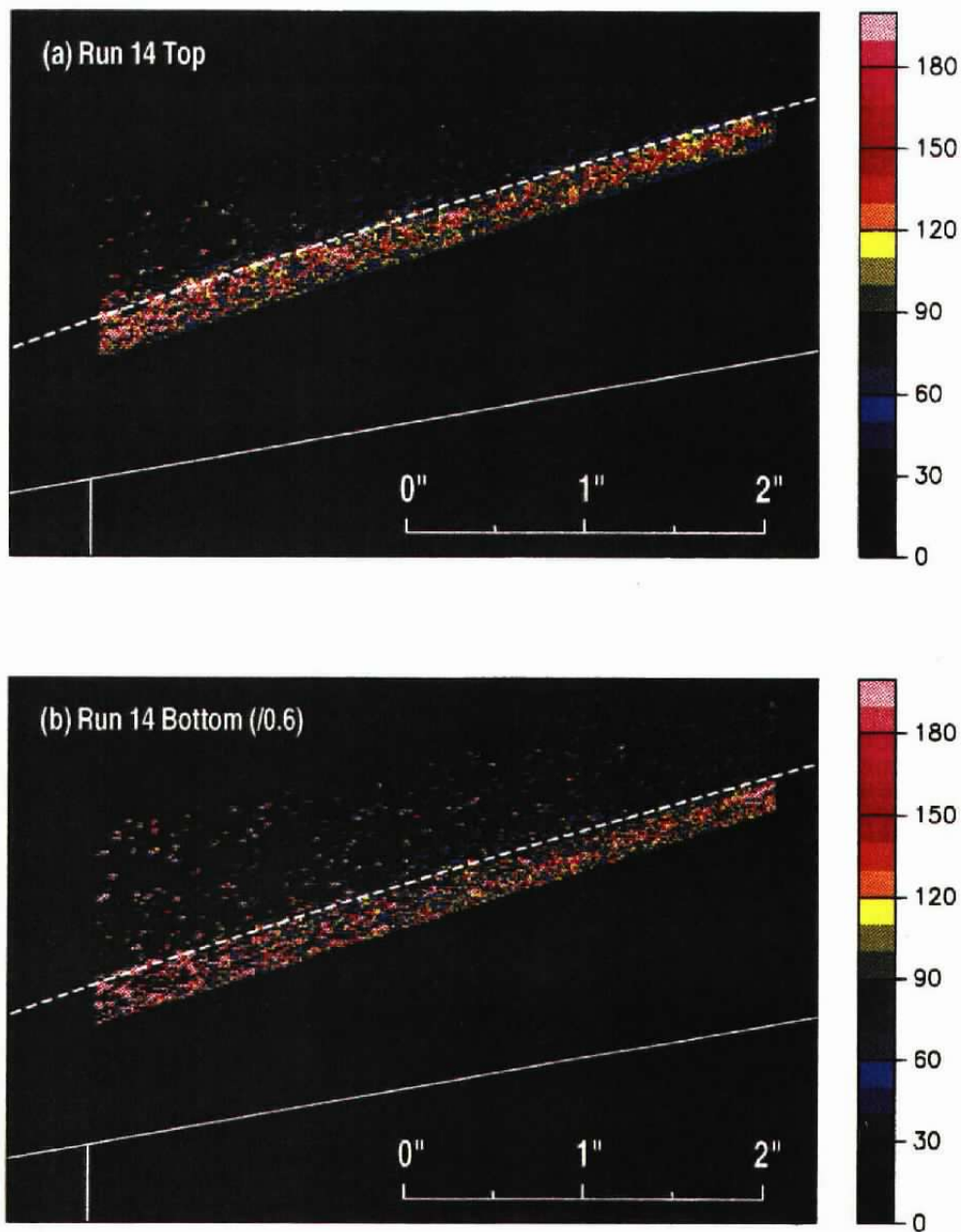


Figure 32. Remapped, energy-normalized PLIF images for Run 14.

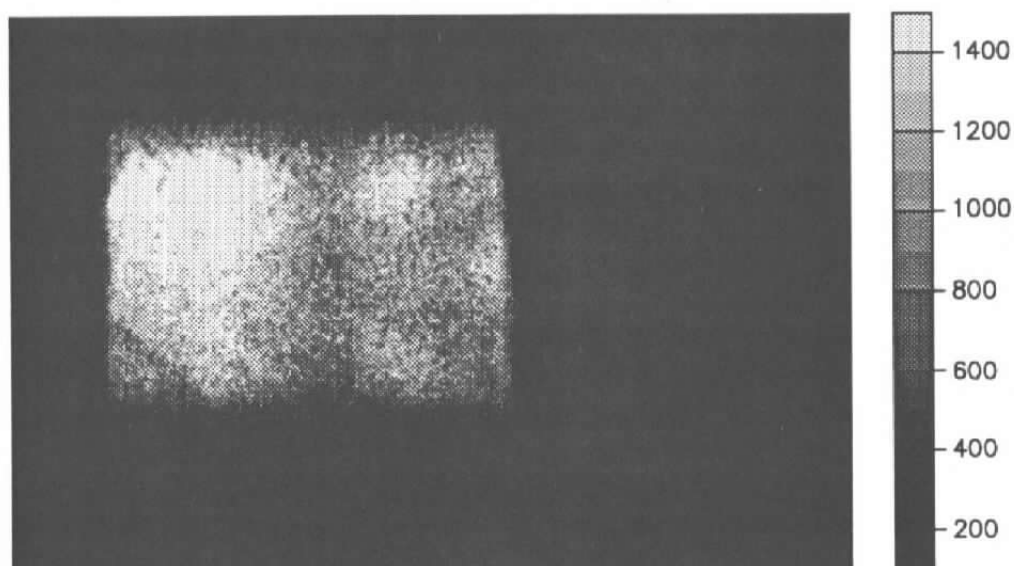


Figure 33. Raw PLIF image for Run 15.

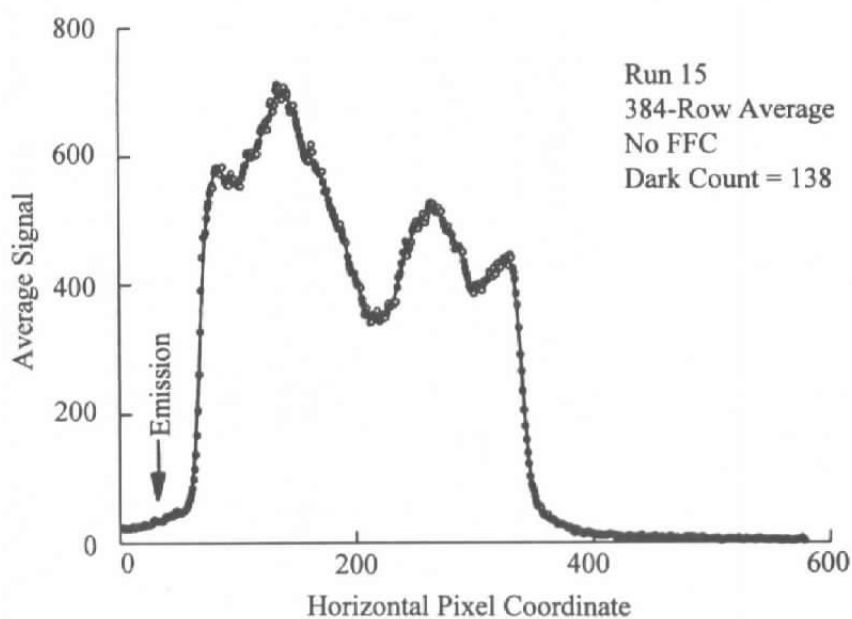


Figure 34. Average horizontal profile of the raw image from Fig. 33.

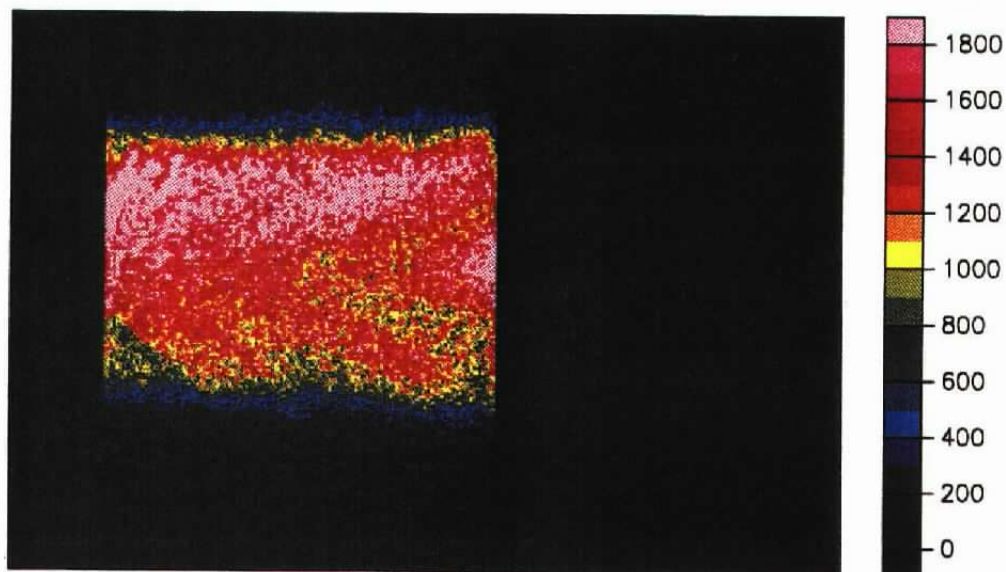


Figure 35. Energy-normalized PLIF image for Run 15.

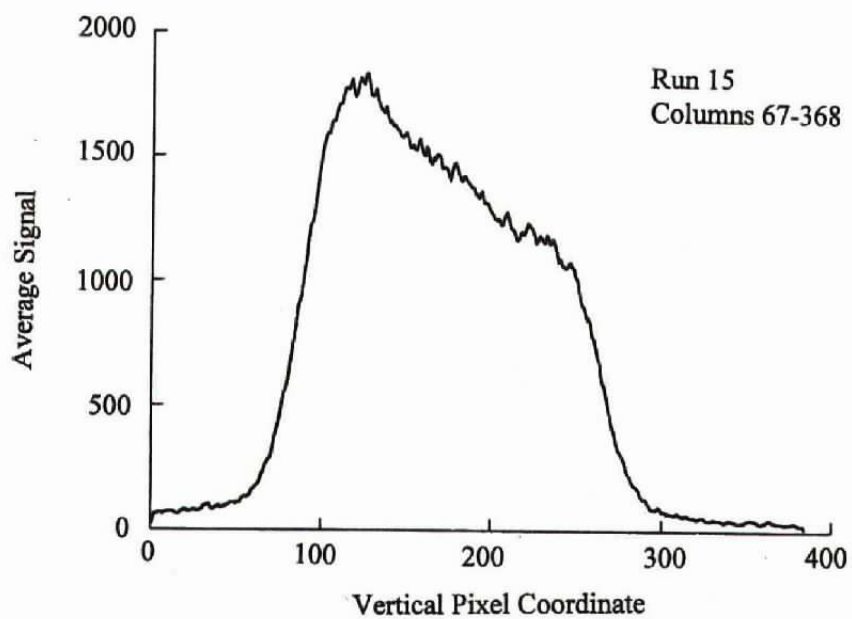


Figure 36. Average vertical profile of the PLIF signal in Fig. 35.

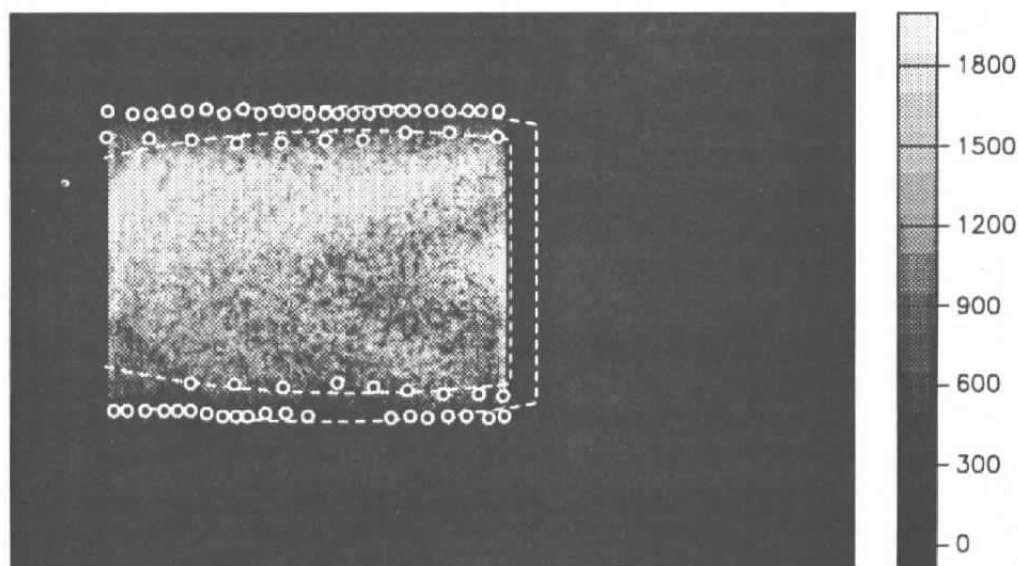


Figure 37. Overlay of selected and fitted intersection points between laser sheet and shock on energy-normalized PLIF image from Fig. 35.

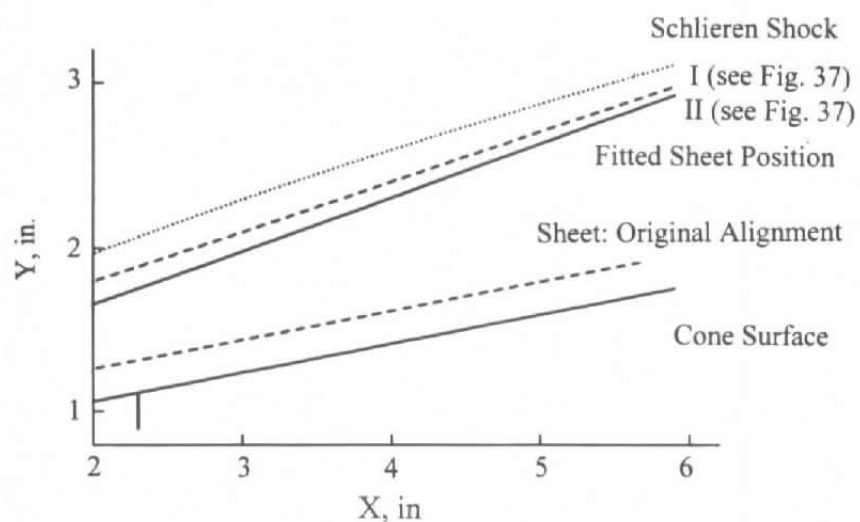


Figure 38. Fitted laser sheet positions for Run 15 shown in test article coordinates.

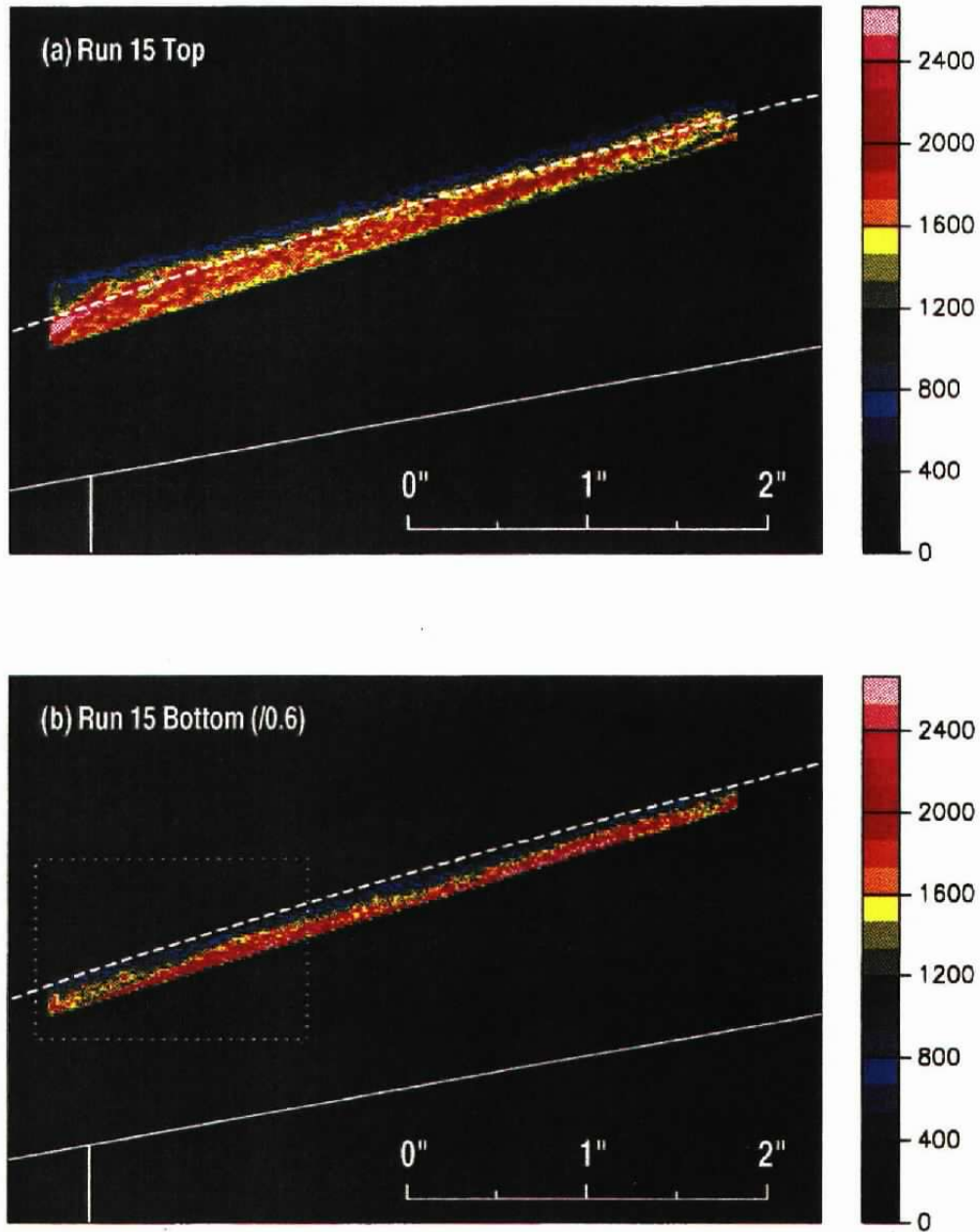


Figure 39. Remapped, energy-normalized PLIF images for Run 14.

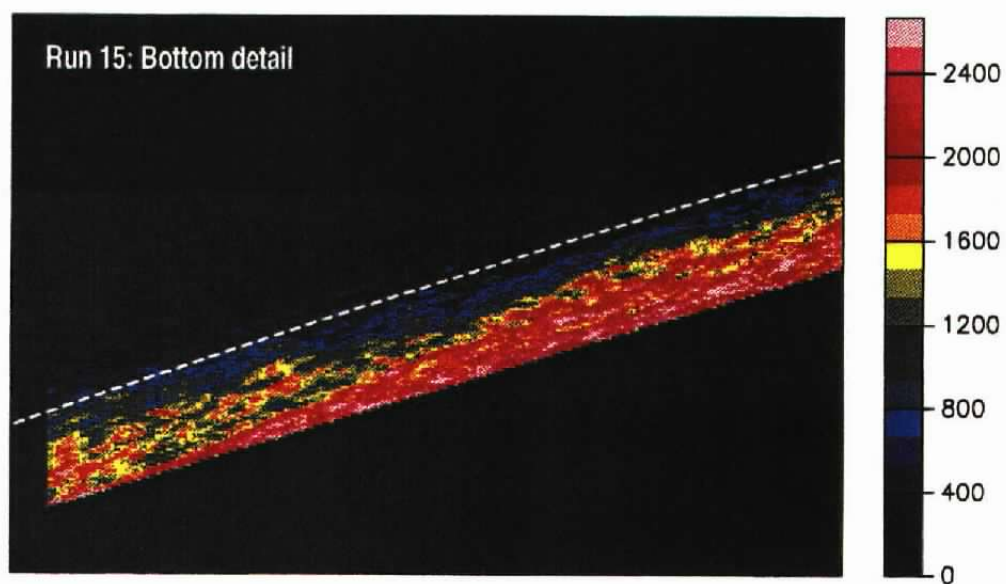


Figure 40. Detail region of Fig. 39b.

Table 1: Fitted Coefficients for Schlieren Shock Positions

	Run 14	Run 15	Run 16
a^*	17.21	18.43	19.34
b^*	0.00242	0.00961	0.01518
c^*	0.00741	0.00196	0.00138
λ	2.71	2.29	2.172

*For x, y in Eq.(2) in mm

NOMENCLATURE

a, b, c	Fit coefficients for schlieren shock position from Eq. (2)
a_s, b_s	Coefficients giving laser sheet position
CCD	Charge-Coupled Device (camera)
CFD	Computational Fluid Dynamics
CFI	Computational Flow Imaging
d	Radial distance between test article surface and laser sheet
D	Distance between camera and camera reference point from Fig. 10
$\hat{e}_x, \hat{e}_y, \hat{e}_z$	Camera unit vectors defined in Eq. (4)
$F^{(i,j)}$	Enclosed fraction of original pixel in remapping from Eq. (7)
i, j	Image pixel indices in remapping process expressed by Eq. (7)
ICCD	Intensified Charge-Coupled Device (camera)
$I_{original}$	Original image pixel intensity from Eq. (7)
$I_{remapped}$	Remapped image pixel intensity from Eq. (7)
p	Zoom factor for camera from Eq. (3)
PLIF	Planar Laser-Induced Fluorescence
R	Nose radius of spherically blunt test article
T^{-1}	Transformation from image coordinates to test article coordinates
\vec{w}	Vector defined in Eq. (5)
x, y, z	Coordinates associated with test article reference frame (Fig. 10)

x_p, y_p	Image pixel coordinates
x_0, y_0, z_0	Coordinates of point at which camera is pointed
α	Half-angle of conical surface of test article
γ	Off-perpendicular camera viewing angle from Fig. 10
δ	Camera pitch angle from Fig. 10
λ	Fit coefficient for schlieren shock position from Eq.(2)
φ	Camera roll angle